Energy & Environmental Science

PERSPECTIVE

In situ TEM electrochemistry of anode materials in lithium ion batteries

Xiao Hua Liu* and Jian Yu Huang*

We created the first nanobattery inside a transmission electron microscope (TEM), allowing for real time and atomic scale observations of battery charging and discharging processes. Two types of nanobattery cells, one based on room temperature ionic liquid electrolytes (ILEs) and the other based on all solid components, were created. The former consists of a single nanowire anode, an ILE and a bulk $LiCoO_2$ cathode; the latter uses Li_2O as a solid electrolyte and metal Li as the anode. Some of the important latest results obtained by using the nanobattery setup are summarized here: (1) upon charging SnO_2 nanowires in an ILE cell with one end of the nanowire contacting the electrolyte, a reaction front propagates progressively along the nanowire, causing the nanowire to swell, elongate, and spiral. The reaction front is a "Medusa zone" containing a high density of mobile dislocations, which continuously nucleate at the moving front and absorbed from behind. This dislocation cloud indicates large in-plane misfit stresses and is a structural precursor to electrochemically driven solid-state amorphization. When the nanowire is immersed in the electrolyte (in a flooding geometry), a multiple-strip-multiple-reaction-front lithiation mechanism operates. (2) Upon charging <112>-oriented Si nanowires, the nanowires swell rather than elongate. We found unexpectedly the highly anisotropic volume expansion in lithiated Si nanowires, resulting in a surprising dumbbell-shaped cross-section, which developed due to plastic flow and necking instability. Driven by progressive charging, the stress concentration at the neck region led to cracking and eventually fracture of the single nanowire into sub-wires. Moreover, the fully lithiated phase was found to be crystalline $Li_{15}Si_4$, rather than the widely believed $Li_{22}Si_5$ phase, indicating the maximum capacity of Si being 3579 mA h g^{-1} at room temperature. (3) Carbon coating not only increases rate performance but also alters the lithiation induced strain of SnO_2 nanowires. The SnO_2 nanowires coated with carbon can be charged about 10 times faster than the non-coated ones. Intriguingly, the radial expansion of the coated nanowires was completely suppressed, resulting in enormously reduced tensile stress at the reaction front, as evidenced by the lack of formation of dislocations. (4) The lithiation process of individual Si nanoparticles was bserved in real time in a TEM. A strong size dependent fracture behaviour was discovered, *i.e.*, there

Center for Integrated Nanotechnologies (CINT), Sandia National Laboratories, 1515 Eubank Blvd. SE, Albuquerque, New Mexico, 87185, USA. E-mail: lxhua99@gmail.com; jhuang@sandia.gov; Tel: +1 (505) 284-5963

Broader context

Lithium ion batteries are widely used in portable electronics because of their high energy density and low weight, and they are currently intensively investigated for more demanding applications such as powering electrical vehicles and for the stationary power backup for fluctuating energy sources such as wind and solar energy. Despite the technical importance and long history of batteries, progress in understanding the science of batteries has been slow. A battery is such a complex device that many concurrent events are occurring during its operation, which makes it difficult to understand the intrinsic electrochemistry. Now with the help of the advanced *in situ* transmission electron microscopy (TEM), the dynamic processes during battery operation can be visualized in real time and with unprecedented high spatial resolution. In this perspective article, we review the progresses in this emerging field with an emphasis on the anode materials of lithium ion batteries, pointing out several ways of improving the *in situ* TEM technique for real time electrochemistry studies, discussing the scientific implications of such *in situ* results on the real design of advanced lithium ion batteries for electrical vehicle applications. Finally, we discuss the possibility of applying the technique to other related fields such as *in situ* corrosion and *in situ* electrodeposition studies.

3844 | *Energy Environ. Sci.*, 2011, **4**, 3844–3860

This journal is © The Royal Society of Chemistry 2011

exists a critical particle size with a diameter of ~150 nm, below which the particles neither cracked nor fractured upon lithiation, above which the particles first formed cracks and then fractured due to lithiation induced huge volume expansion. For very large particles with size over 900 nm, electrochemical lithiation induced explosion of Si particles was observed. This strong size-dependent fracture behaviour is attributed to the competition between the stored mechanical energy and the crack propagation energy of the nanoparticles: smaller nanoparticles cannot store enough mechanical energy to drive crack propagation. These results indicate the strong material, size and crystallographic orientation dependent electrochemical behaviour of anode materials, highlighting the powerfulness of *in situ* TEM electrochemistry, which provides not only deep understanding of the fundamental sciences of lithium ion batteries but also critical guidance in developing advanced lithium ion battery for electrical vehicle and backup power for fluctuation energy sources such as wind and solar energy.

1. Introduction

Lithium ion batteries (LIBs) are widely used in portable electronics because of their high energy density and low weight. However, to meet the more demanding applications such as powering electrical vehicles and for the stationary power backup for fluctuating energy sources such as wind and solar energy, new cathode and anode materials with much higher energy density and power density, better cyclability, and safer operating conditions than the existing ones need to be developed.[1–13] Current LIBs use carbonaceous materials as anode, with a theoretical energy density of 372 mA h g^{-1} for graphite. A number of materials such as aluminum (Al),[14,15] tin (Sn),[9,16] germanium (Ge),[17,18] and silicon (Si),[19–23] *etc.*, have much higher energy storage capacity of being 993, 993, 1384, and 3579 mA h g^{-1}, respectively, than that of carbon. However, a major issue with these high energy density anode materials *via* the alloying mechanism is that they experience large volume changes in the first cycle, leading to cracking, fracture, in turn capacity fading and failure of batteries.[24] A fundamental understanding of the structure instability of electrode materials during cycling is important and can provide strategies to mitigate the mechanical failure. In this context, a number of *in situ* techniques are being developed to follow the structural evolution of electrode materials during cycling. Some important *in situ* techniques include:

optical microscopy,[25,26] scanning electron microscopy (SEM),[27–32] synchrotron X-ray diffraction (XRD),[33–42] synchrotron X-ray absorption spectroscopy (XAS),[33,43–46] synchrotron transmission X-ray microscopy (TXM),[16] Raman spectroscopy,[47,48] Fourier transform-infrared spectroscopy (FTIR),[49,50] mass spectroscopy (MS),[50–56] and nuclear magnetic resonance (NMR) spectroscopy.[57–60] Optical microscopy offers too poor a resolution to yield useful microstructural evolution information during battery cycling. SEM has much better spatial resolution (down to 1 nm scale) than optical microscopy, and can provide useful morphology evolution, such as micro-cracking of particles during battery cycling, but SEM operates in a high vacuum, and special designed cells need to be implemented. *In situ* XRD provides excellent collective crystal structure information, and *in situ* XAS provides electronic structure changes such as charge transfer during cycling. Also *in situ* XRD and *in situ* XAS do not require placing the electrochemical cell in a high vacuum, which makes these techniques very useful for monitoring an electrochemical cell in a real battery configuration. *In situ* TXM shows much better spatial resolution than those of the *in situ* XRD and XAS, and the former also provides the bulk information rather than only the surface morphology changes provided by SEM. The nondestructive analytical tools, such as FTIR, MS, and NMR, are also widely used to probe the

Xiao Hua Liu received his BS from Department of Materials Science and Engineering in Tsinghua University in 2003 and his PhD from Beijing National Center for Electron Microscopy (BNCEM) in Tsinghua University in 2008. His research interests include nanoscale materials for renewable energy, energy storage, and dynamic transmission electron microscopy.

Xiao Hua Liu

Jian Yu Huang received his BS from Xiangtan University in 1990 and PhD from Institute of Metal Research, Chinese Academy of Sciences in 1996. His primary research interests are centered on in situ electron microscopy of nanostructured materials. He intends to bridge the gap between microstructure characterizations and property measurements by conducting integrated studies on the microstructure and electrical, mechanical, thermal and electrochemical properties of individual nanostructures, such as carbon nanotubes, nanowires, and nanoparticles.

Jian Yu Huang

interfacial processes and volatile products during battery operation, such as decomposition of electrolyte,[49] generation of gaseous substances,[50,51,56] formation of solid electrolyte interface (SEI),[49] formation of metallic dendrite,[57] *etc.* Some other techniques for studying LIBs include: atomic force microscopy (AFM),[61,62] and scanning tunneling microscopy (STM).[63,64]

In situ transmission electron microscopy (TEM) has been extensively used in material science to conduct real time structure and properties measurements,[65–78] but *in situ* TEM battery studies have not been possible until very recently.[79–88] This is because conventional LIBs usually use liquid electrolytes, which cannot be placed into the high vacuum TEM column directly. Liquid cells consisting of top and bottom silicon nitride membranes sealing the liquid are thus developed.[89–92] The liquid cell provides useful information about the morphology evolution of nanoparticle growth or grain growth during electrochemical plating, but the spatial resolution is limited, similar to SEM, and also it is not easy to perform real time composition analysis. There are attempts to fabricate all-solid electrochemical cells to enable *in situ* studies of cycling,[93,94] and it appears to be successful in the very recent experiments.[94]

We recently successfully created the first working nanobattery inside the TEM using an "open-cell" concept, which differs completely from the conventional sealed liquid cell approach.[79] Our open cell nanobattery consists of a single nanowire anode with diameter less than 200 nm, an ionic liquid electrolyte (ILE), and a bulk $LiCoO_2$ as the cathode. The setup utilizes the advantage of the ultra low vapor pressure of an ionic liquid, which is essentially a molten salt and survives the high vacuum of a TEM.[79,86,87,95,96] The advantages of the open-cell nano-battery are: allowing truly real time and atomic scale resolution microstructure investigation, and concurrent nanometre to atomic scale composition analysis, which have not been achieved in any previous technique and represent a milestone in the *in situ* TEM electrochemistry field. Besides direct observation of morphology evolution, analytical TEM provides complete structure information through electron diffraction patterns (EDPs), electronic structure and chemical information through electron energy loss spectroscopy (EELS), and straightforward compositional information through energy dispersive X-ray spectroscopy (EDS).

In this paper, we review our recent progress in the *in situ* TEM electrochemistry of anode materials in LIBs,[80–85,88] and then provide a perspective of the application of this new technique to explore new cathode and anode materials.

2. Methodology

The major technical difficulty for conducting an *in situ* electrochemical experiment in a TEM is to introduce a liquid electrolyte into the TEM column with a typical vacuum level of 10^{-5} Pa

(10^{-7} Torr). Table 1 lists the room temperature vapour pressures of the most widely used solvents, such as ethylene carbonate (EC), propylene carbonate (PC), dimethyl carbonate (DMC), and diethyl carbonate (DEC), which are 5–8 orders of magnitude higher than the TEM column pressure.

A sealed cell, which uses electron transparent thin membranes to separate the volatile liquid electrolyte from the high vacuum, can be fabricated for *in situ* TEM observations of electrochemical reactions.[89–92] The advantages of this design include: (1) universal compatibility with theoretically any electrolyte; and (2) a thin liquid layer on the electron beam path enabling "see-through" the reactions immersed in the electrolyte. However, the disadvantages are also obvious: (1) much work is required on high-precision nanofabrication; (2) little flexibility for analytical TEM techniques and manipulation of the active materials; (3) risk of leakage; (4) the poor image contrast and resolution due to the thick liquid, and (5) difficult to perform composition analysis.

Alternatively, an open cell can be constructed by using vacuum-compatible electrolytes, *i.e.*, an ILE with a negligible vapour pressure,[96] or a Li-containing solid-state electrolyte (SSE).[94] Fig. 1 shows the schematic illustrations of the three types of electrochemical devices used in our experiments, *i.e.*, a liquid cell using ILE (Fig. 1a), a solid cell using naturally grown Li_2O layer as the SSE (Fig. 1b), and a solid cell using LiAlSiO SSE coated on the nanowires (Fig. 1c). When using Li_2O layer as the solid electrolyte, a -2 V bias is usually required to drive the Li^+ through the Li_2O layer.

The other key component and advantage of the open-cell design is the precision positioning capability. Unlike the "fixed" configuration in the sealed cell after loading samples, the open cell offers large room and great flexibility for manipulation and analytical characterization techniques. The piezo-positioner used in the experiments described below is a TEM-STM holder (Nanofactory®).[98] In an experiment, one terminal is driven by the positioner to approach the other at fine steps, thus a single nanoparticle or nanowire can be attached to one electrode for the lithiation/delithiation tests. And bulk materials, such as multiple nanowires/nanoparticles or thin films can also be studied in the same manner.

Another critical advantage of our nanobattery setup is that only the active materials are charged and discharged, allowing for real time intrinsic electrochemistry probing. A real battery system is usually complicated by the complex components such as binder, carbon coating, and additives, which is very difficult to decouple all effects or to understand the true electrochemistry of the active materials.

2.1. Liquid cell

The ILE was made by dissolving the lithium salt, lithium bis(trifluoromethylsulfonyl) imide (LiTFSI), in a solvent of 1-butyl-1-methylpyrrolidinium bis(trifluoromethylsulfonyl) imide (P_{14}TFSI) at the concentration of 10 wt% LiTFSI. Table 2 lists the main physical properties of the solvent, P_{14}TFSI.[95] In a typical experiment, one drop of the ILE was placed on the top surface of the $LiCoO_2$ bulk, which was glued to an Al rod. On the other side, nanowires were glued to another Al rod with conductive epoxy (Fig. 1a). For different materials, the exact device structure may be modified to ensure the best performance,
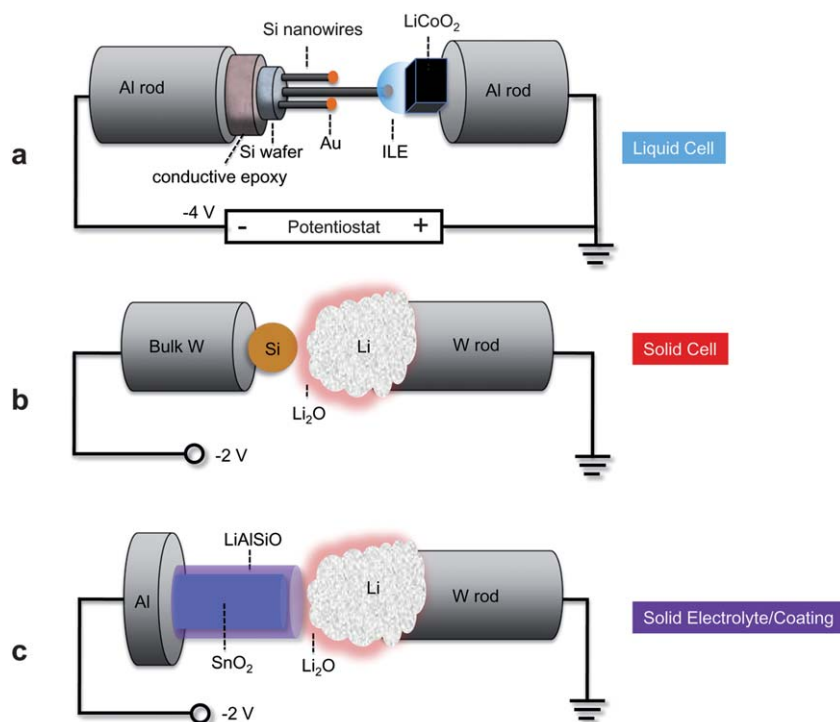
Table 1 Vapour pressure of solvent around room temperature[97]

Solvent (formula)	Vapour pressure/Pa
Ethylene carbonate ($C_3H_4O_3$)	1.33 (20 °C)
Propylene carbonate ($C_4H_6O_3$)	4 (25 °C)
Dimethyl carbonate ($C_3H_6O_3$)	5300 (20 °C)
Diethyl carbonate ($C_5H_{10}O_3$)	1400 (25 °C)

Fig. 1 Schematic illustrations of the open cell nanobattery setup inside a TEM, enabling *in situ* TEM electrochemical experiments. One electrode of the two-terminal devices is connected to a piezo-positioner. A negative or positive potential is applied to the fixed terminal with respect to the mobile terminal for lithiation or delithiation, respectively, after the contact is established. (a) Liquid cell. As an example, one drop of the ILE is placed on the tip of the $LiCoO_2$ bulk, while long objects such as Si nanowires can be used as the anode. (b) Solid cell. Li metal is used as the reference electrode and lithium source, while a naturally formed thin Li_2O layer on the Li metal serves as a solid-state electrolyte allowing Li^+ transport. Small objects of interest, like individual Si nanoparticles, are more suitable for this device configuration. (c) Solid cell with additional solid electrolyte. The ion-conducting LiAlSiO layer can be replaced by other materials of interest, such as a carbon layer as an electronic conductor, *etc.*

Table 2 Physical properties of $P_{14}TFSI$[95]

Property	Value
Glass transition temperature	$-87\ ^{\circ}C$
Melting point	$-18\ ^{\circ}C$
Fluid density	$1.41\ g\ ml^{-1}$ (20 $^{\circ}C$)
Fluid conductivity	$0.22\ S\ m^{-1}$ (25 $^{\circ}C$)
Fluid viscosity	$0.085\ Pa\ s$ (25 $^{\circ}C$)
Electrochemical window	> 5.5 V (25 $^{\circ}C$)

for instance, we have found that using the cleaved Si wafer with the Si nanowires directly grown on it provides most reliable electrical contact between the semiconducting Si nanowires and the current collector.[80]

The liquid cell resembles a real but miniaturized LIB with the necessary components except for packaging. Fig. 2 shows an interesting phenomenon of liquid beads shooting, demonstrating the high fluidity of the electrolyte in the vacuum environment. Fig. 2o shows a typical image of the ILE layer wetted nanowire. Due to the high fluidity and surface tension force, long objects, such as nanowires with high aspect ratio, are more suitable for this liquid cell setup.

One of the key technical issues with the liquid cell is the electron beam induced degradation of the ILE. Experimentally, a critical electron dosage was found to be $\sim 10^{-3}$ A cm^{-2}, below which the ILE exhibited long lifetime during the experiment.

At high electron beam intensity, the ILE cures quickly and forms jelly coatings on the nanowire surface, resulting in loss of Li^+ transport capability.

The other challenge associated with the liquid cell is the opaqueness of the ILE under the electron beam. The reactions ongoing in the immersed part of a nanowire are not instantly visible, unless the nanowire is periodically pulled out of the ILE and checked.[84] Nevertheless, due to the large mass ratio between the electrolyte, the cathode and the single nanowire anode, the change of the potential in the cathode during charging is negligible, and the heating effect to the nanowire is also avoided because the ILE acted as a heat sink.[82]

2.2. Solid cell

In the solid cell (Fig. 1b), Li metal is the lithium source, and the native Li_2O layer formed on the metal surface acts as a solid electrolyte permitting Li^+ transport but not electron transport. Li_2O is naturally formed on the fresh Li metal that is briefly exposed to the air (for ~ 2 s) when the holder is inserted into TEM. Structural analysis has revealed a typical thickness of ~ 700 to 1000 nm of the Li_2O layer. Due to its large band gap of ~ 8 eV,[99] Li_2O is electrically insulating. To promote the Li^+ ion transport through this layer, sufficient potential of ~ -2 V is necessary to initiate the Li^+ diffusion. Although Li_2O is seldom used as an electrolyte in conventional LIBs, it is a common component of the SEI layer. Furthermore, our previous results
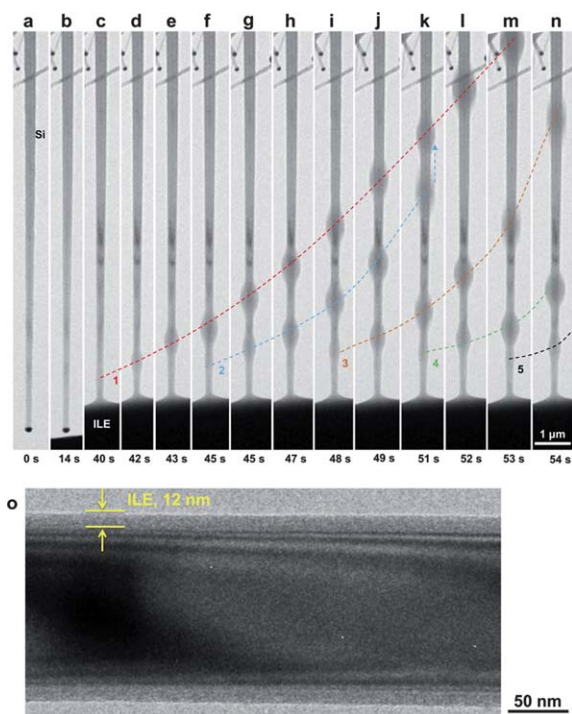
Fig. 2 Flowing of the ionic liquid on a Si nanowire in vacuum without applying bias. Time-elapsed images showing the liquid beads shooting from the ILE reservoir towards the nanowire root. The dashed lines show the trajectory of five sequentially generated beads (marked by "1" to "5"). Note that Bead 2 caught up with and merged into Bead 1 in panel (k). (o) High magnification image showing the 12 nm thick ILE layer on the surface of a nanowire.

show that Li_2O is indeed a Li^+ conductor with a potential barrier of only 0.4 eV, and the diffusivity of Li^+ in Li_2O is about 10^{-10} cm^2 s^{-1}. Our experimental results have indicated sufficient Li^+ transport capability of nanoscale Li_2O.[79,81]

Many of our experiments have demonstrated that the Li_2O layer is indeed a good Li^+ conductor but not electron conducting, thus charging and discharging experiments were successfully conducted in many anode materials.[81,85] A solid cell is beneficial for fundamental studies of the lithiation behaviour of a nano-object for two reasons. First, the entire object is visible in the entire electrochemical process. Second, small objects such as nanoparticles with size down to a few nanometres can be cycled and imaged in real time, which is not possible in a liquid cell because the ILE will cover the entire particle, making it impossible to image. Although differing more from a real battery than the liquid cell, the solid cell offers complete structural information from the very beginning of lithiation. Fig. 1b shows the schematic illustration of lithiating a Si nanoparticle between the bulk W and Li metals.

It is noted that the Li_2O is very sensitive to the electron beam,[100,101] strong e-beam dose decomposes Li_2O directly to Li and O, $2Li_2O \rightarrow 4Li + O_2\uparrow$, and we were able to chemically lithiate nanoparticles by using this e-beam decomposition technique without applying any potential to the nanoparticles. Interestingly, the chemical lithiation of Si nanoparticles shows almost the same characteristic as that of the electrochemical lithiation.[85]

Depending on the purpose of research, different structures can be configured for the *in situ* electrochemical tests. Fig. 1c shows the incorporation of a LiAlSiO solid-state electrolyte on the SnO_2 nanowire. The coating layer could be any other materials for the setup, for instance, a carbon layer, to study the lithiation behaviour of a nano-composite electrode.[83]

3. Lithiation behaviour of various anode materials

Using the nanobattery setups introduced above, we have been studying several model material systems, such as oxides (SnO_2, ZnO, Fe_2O_3), pure metals (Al, Sn), semiconductors (Si, Ge), carbonaceous allotropes (graphene nanosheets, carbon nanotubes, graphite), and metal sulfides (Co_9S_8, Ag_2S), *etc.* It turned out that each material behaves differently from the others, although some common features exist for the lithiation behaviours. This observation highlights the power and necessity of conducting *in situ* electrochemistry to reveal the underlying material-specific properties. Some representative results are summarized in the following.

3.1. *In situ* lithiation of tin oxide (SnO_2) nanowires

SnO_2 has the theoretical capacity of 781 mA h g^{-1},[102] twice that of graphite. Upon lithiation, SnO_2 undergoes electrochemically driven solid-state amorphization (ESA) process, forming elongated and twisted morphology (Fig. 3a–d). The reaction front propagates towards the nanowire root along the nanowire axial direction.[79] Close views of the reaction fronts reveal large volume expansion and high stress, characterized by the high dislocation density zone or so-called "Medusa zone" (Fig. 3e), or cracked zone (Fig. 3f) between the single-crystalline SnO_2 part and the lithiated amorphous region. The dislocations are generated due to the volume mismatch in the interface between the lithiated segment and the pristine nanowire. The reaction can be expressed by the following two-step mechanism:

$$SnO_2 + 4Li^+ + 4e^- \rightarrow Sn + 2Li_2O \qquad (1)$$

$$Sn + xLi^+ + xe^- \leftrightarrow Li_xSn \qquad (2)$$
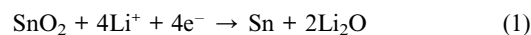
The first step is irreversible, leading to formation of metallic Sn particles dispersed in the amorphous Li_2O matrix (Fig. 3g). The second step is reversible. The formation of a Sn and Li_2O composite is beneficial to improve the mechanical stability and cyclability of the Sn nanoparticles, which otherwise coalescence into big Sn particles, resulting in rapid capacity fading.[103]

The electrochemical reaction leads to significant geometry changes of the nanowire: about 45% diameter increase, 60% elongation, in total accounting for about 240% volumetric expansion.[79] The significant elongation is unexpected, as it is generally believed that the nanowire swells rather than elongate. This demonstrates the importance of *in situ* study to reveal the intrinsic electrochemical process of the active materials, which cannot be obtained by other experimental techniques.

When one end of the nanowire contacts the electrolyte (hereafter refer to end-contact), the lithiation occurred along the longitudinal direction with a single reaction front above the ILE surface, it is expected that the lithiation mechanism in the
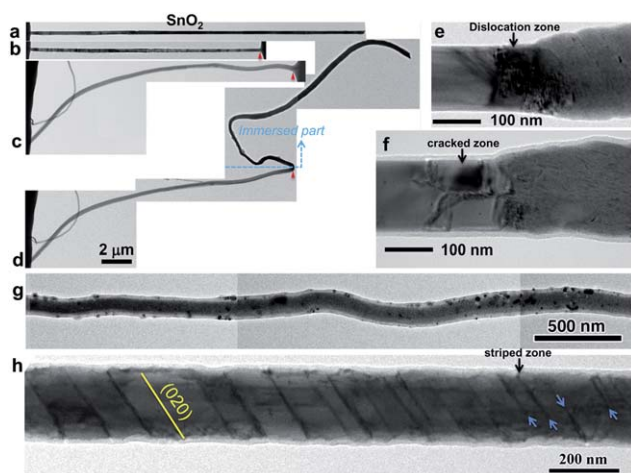
Fig. 3 Lithiation of a SnO_2 nanowire with either one end contacting the electrolyte (end-contact) or the entire nanowire immersed in the electrolyte (flooding geometry). A potential of -3.5 V to -3 V was applied to the nanowire against the $LiCoO_2$ cathode. (a) Pristine SnO_2 nanowire with a uniform diameter and a straight shape. The nanowire is a single crystal with the growth direction of [011]. (b) The nanowire was partially immersed in the ILE. The red triangle marks the position of the ILE surface. (c) Elongated, thickened, and curved segment above the ILE surface after lithiation. (d) Full morphology showing a similar swelled segment of the immersed part after the ILE was retracted. (e) Typical morphology of the single reaction front above the ILE surface. There is a highly strained zone with high density of dislocations that separates the non-reacted SnO_2 nanowire from the lithiated amorphous part. (f) Another morphology showing crack formation in the reaction front instead of the more commonly observed dislocation zone shown in (e). (g) Typical morphology of the lithiated SnO_2 nanowire with a curved shape and dark Sn precipitates in the amorphous Li_2O matrix. (h) Typical intermediate state with the formation of multiple stripes along the (020) planes in SnO_2 nanowires lithiated in a flooding geometry. Preferential Li insertion into these planes leads to formation of the multiple stripes, which serve as multiple reaction fronts that expand laterally to complete the amorphization/lithiation process in a flooding geometry.[79,84] Reproduced with permission from the American Association for the Advancement of Science.

immersed part in a flooding geometry may be different. Understanding lithiation mechanism in a flooding geometry is important, because in a real battery system, the active materials are always flooded with an electrolyte, thus the flooding geometry lithiation mechanism may better reflect what's occurring in a real battery system. Fig. 3h shows the unique multi-stripe morphology when the flooded segment of a SnO_2 nanowire was pulled out.[84] Crystallographic analysis shows that the stripes were parallel to the (020) planes, along which the Li^+ ions were inserted. The blue arrows mark the half-traversed stripes as intermediate state, indicating the strips nucleated from surface, possibly from surface defects, and then propagated along the (020) planes to the other side of the nanowire. Unlike a single reaction front migration, the SnO_2 nanowire was lithiated through a multi-stripe-multi-reaction-front manner, *i.e.*, many stripes served as the simultaneous reaction fronts, which expanded laterally by converting the adjacent crystalline SnO_2 phase into amorphous phase.[84] The multi-stripe-multi-reaction-front lithiation mechanism was not observed in the end-contact geometry, and the reason for this is not understood. It was

expected that the lithiation rate in a flooding geometry is much faster than that in the end-contact configuration, which was indeed the case in our experiments: in the former, it usually took less than 5 min to lithiate the entire nanowire, while in the latter it usually took at least half an hour to complete the lithiation. Although the initial material (SnO_2) and final products (Li_2O, Li_xSn, Sn) are the same for both end-contact and flooding geometry, the detailed mechanisms are indeed quite different.

These results demonstrate that SnO_2 nanowires can sustain high lithiation stress without fracture because the dislocations easily run out to the nanowire surface, indicating nanowires indeed have the advantage of facile stress release over bulk materials as electrodes.

3.2. *In situ* lithiation of Si nanowires

Si has the highest theoretical capacity among all anode materials, namely 3579 mA h g^{-1} for $Li_{15}Si_4$ observed in room-temperature electrochemical cells and 4212 mA h g^{-1} for $Li_{22}Si_5$ at high temperatures.[19,60,104–106] It is a promising candidate for high energy anode of LIBs, thus are attracting much attention. The transformation from the crystalline Si to $Li_{15}Si_4$ phases accounts for a volume expansion of 281%.[36,107,108] As a result, fracture and pulverization caused electrical contact loss are believed to be the root cause for the rapid capacity fading, and finally failure of the Si-based electrodes.[23,104] Although numerous papers in the literature reported different lithiated Li_xSi phases and cycling performance, there is a lack of a fundamental understanding of some important issues, such as what the fully lithiated phase is for Si at room temperature, and what mechanical effects are accompanying the electrochemical lithiation process, *etc.* Understanding the lithiation mechanism at the atomic scale is challenging, although recent *in situ* NMR studies provided important insights into the atomic scale lithiation/delithiation mechanisms,[58,60] and some *in situ* optical microscopy and XRD studies showed colossal volume changes and phase transformations during cycling.[109,110] Our *in situ* TEM studies provided further direct evidence of the atomic scale lithiation mechanism of Si.

Fig. 4 shows the ESA process of an intrinsic Si nanowire. The pristine Si nanowire was straight and with uniform diameter, and the growth direction is [112] (Fig. 4a). After lithiation, it formed a crystalline-core–amorphous-shell structure, indicating that the lithiation occurred from the nanowire surface towards the centre (Fig. 4c–g) with the phase transformation from single crystalline Si (*c*-Si, Fig. 4h–i) to amorphous Li_xSi (*a*-Li_xSi) alloy in the lithiated shell, and there exists a conical residual unlithiated *c*-Si core even after prolonged lithiation (Fig. 4j–k). The EDP of *a*-Li_xSi has two characteristic diffuse and broad rings (Fig. 4j), corresponding to the *d*-spacing of 4.4 to 3.3 Å and 2.2 to 1.8 Å, respectively. Fig. 4k shows the schematic illustration of the core–shell lithiation mechanism for the segment above the ILE surface. As the reaction front propagated, Li ion flux was transported through the thin ionic liquid layer on the nanowire surface; meanwhile, the Li ions were injected into the Si lattice radially, converting the shell into *a*-Li_xSi alloy. It is worth noting that the residual *c*-Si core, indicating incomplete lithiation even for prolonged reaction, was only seen for the intrinsic Si nanowires but not for phosphorus-doped or carbon-coated Si nanowires with higher electronic conductivity.[80] It is very likely that very small Si
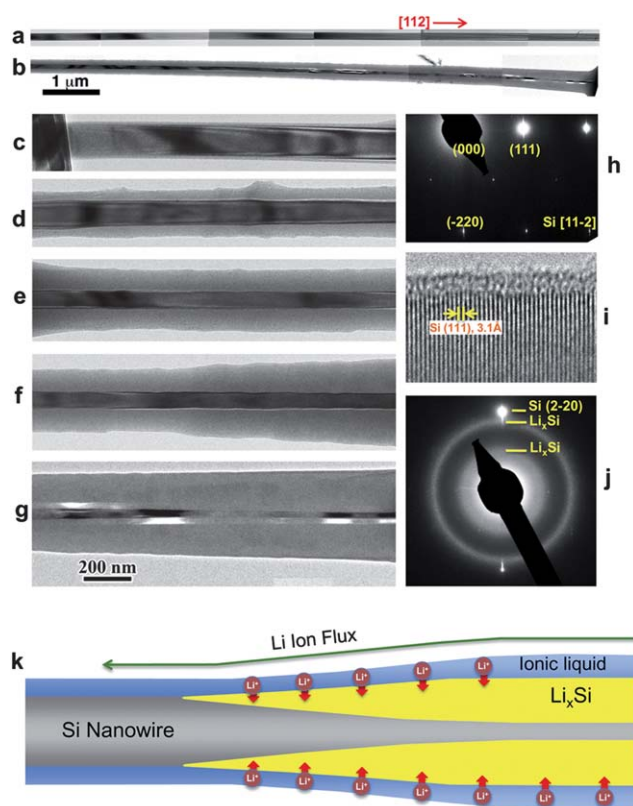
Fig. 4 Core–shell lithiation manner of a [112]-oriented intrinsic Si nanowire. A potential of −4 V was applied to the nanowire against LiCoO₂. (a) Pristine Si nanowire with a uniform diameter and a growth direction of [112]. (b) Core–shell structure of the lithiated nanowires. (c–g) High magnification images of the different segments of the nanowire shown in (b), showing progressive lithiation from the nanowire surface towards the centre, forming a conical-shaped c-Si core and a gradually thickening lithiated shell. (h) Electron diffraction pattern (EDP) showing single crystalline structure of the pristine Si nanowire. (i) High resolution image showing the (111) lattice fringes of the pristine Si nanowire with a thin layer of amorphous silicon oxide of about 1.5 nm on the surface. (j) EDP of the lithiated Si nanowire showing the diffuse bands from the a-Li$_x$Si shell superimposed on the sharp spots from the residual c-Si core. (k) Schematic illustration of the core–shell lithiation manner of ⟨112⟩-oriented Si nanowires. Reproduced with permission from the American Chemical Society.

nanowires have poor electrical conductivity due to surface charge depletion, highlighting the importance of improving the electrical conductivity on rate and capacity enhancement. For the ⟨112⟩-oriented Si nanowires, the core–shell lithiation manner was observed in a flooding geometry,[80] resulting in radial expansion but little elongation, which is significantly different from the axial or multi-stripe lithiation manners observed in SnO₂ nanowires (Fig. 3). Also in the lithiation of Si nanowires, there was no dislocation in the reaction front, highlighting that lithiation behaviour is very material dependent.

3.3. Doping and coating effects on lithiation of Si and the formation of crystalline Li$_{15}$Si$_4$ final phase

Doping and carbon coating (or compositing with other conductive materials) are two important techniques that have

been widely used in LIBs to improve the rate and capacity.[5,111–118] The charging rate of intrinsic Si was very slow, furthermore, we were not able to fully lithiate intrinsic Si nanowires even after prolonged lithiation time due to its intrinsic poor electrical conductivity, in this context, we conducted lithiation experiments of three additional different samples, *i.e.*, carbon-coated (C-coated), phosphorus doped (P-doped), and C-coated plus P-doped Si nanowires to compare with the charging behaviour of intrinsic Si nanowires.[80,119] Fig. 5 shows the typical microstructure evolution of a P-doped and C-coated Si nanowire in the first lithiation/delithiation cycle. The pristine c-Si nanowire (Fig. 5a) was converted to the crystalline Li$_{15}$Si$_4$ (c-Li$_{15}$Si$_4$) phase (Fig. 5b, d) after lithiation, and then converted to amorphous Si (a-Si) after delithiation (Fig. 5c and e). Fig. 5f shows a snapshot of the reaction front with some important features, *i.e.*, the core–shell structure at the reaction front, large volume expansion, and the spiral shape of the lithiated nanowire. It is noted that the spiral shape was formed in nanowires with fast charging speed, *e.g.*, the P-doped and C-coated nanowires, indicating the very ductile nature of the lithiated product, which is in contrast to the brittle nature of intrinsic Si nanowires. The major effects of improving the electrical conductivity by P-doping or C-coating can be summarized as follows (Fig. 5g): (1) enhancing charging rate, carbon coating and P doping each leads to 3 to 4 orders of magnitude increase in the electrical conductivity, and in turn, each leads to 1 order of magnitude increase in the charging rate (measured by the moving speed of the reaction front) as compared to the intrinsic Si nanowires. The fastest charging rate was observed in the C-coated and P-doped nanowires. We observed full lithiation of a P-doped and C-coated Si nanowire in seconds, highlighting great promise of designing high power Si electrodes by nanoengineering;[80] (2) complete lithiation to the c-Li$_{15}$Si$_4$ phase instead of the a-Li$_x$Si phase and without a residual c-Si core.[80] These results also indicate that C-coating and P-doping play equivalent role in enhancing the charging rate and capacity of LIBs.[5,111] These results point to the important direction on how to improve the energy density and powder density Si anode in a LIB.

It should be noted that the doping and carbon coating effects are most significant in the first cycle, but not as dramatic in the following cycles. However, rate improvement was still observed in the following cycles. Also we noted that the carbon coating layers showed dramatic breathing behaviour, namely expanding and shrinking simultaneously with that of the Si nanowires during lithiation and delithiation, respectively, without breaking if the coating layer thickness is less than 10 nm. The coating layer broke on the first lithiation if its thickness was over 10 nm. These results imply that a thinner coating layer has much better flexibility to follow the volume changes of the inner Si material than a thicker one.

Based on the electron diffraction analyses from many C-coated, or P-doped, or C-coated and P-doped Si nanowires, Li$_{15}$Si$_4$ was the only final crystalline phase observed after lithiation under various conditions, such as in both the liquid and solid cells. Fig. 5h shows a typical electron diffraction pattern from the fully lithiated Si nanowire along with the simulated diffraction rings with intensity distribution, showing excellent agreement between the experimental and the simulation results. The EDP is characterized by two groups of sharp rings: the inner
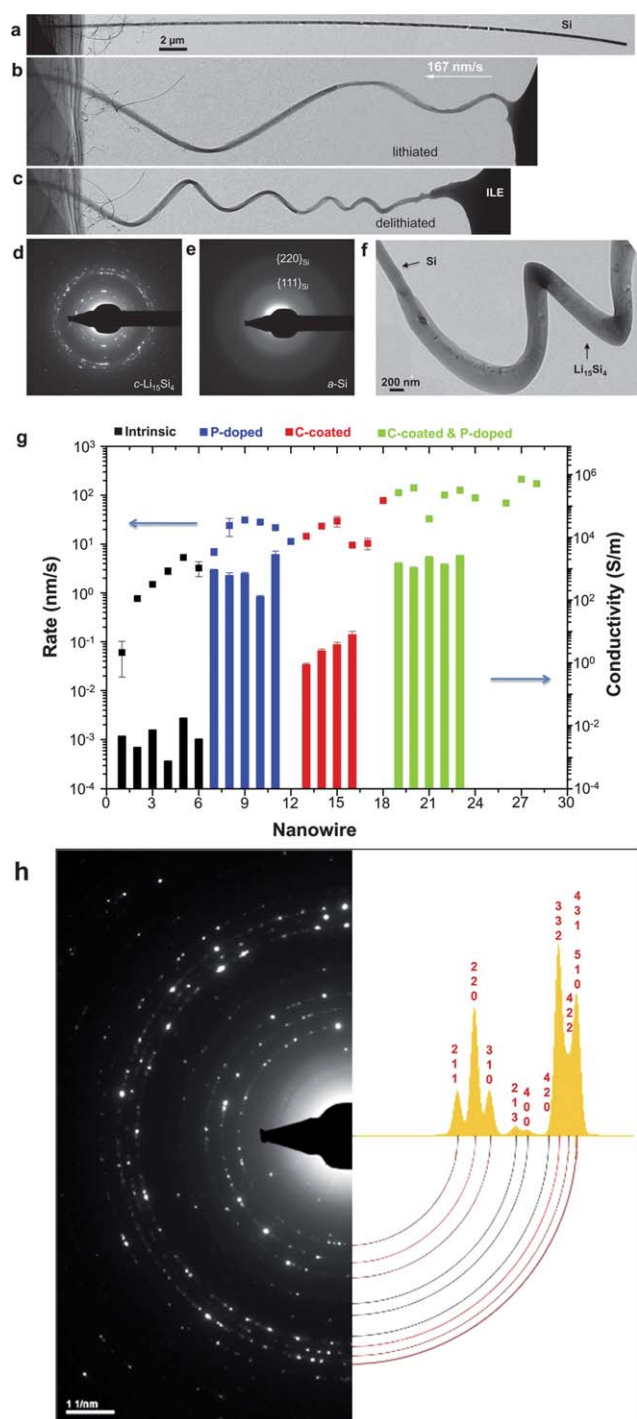
group with *d*-spacing of 4.350 to 3.369 Å (from {211} to {310} planes) and the outer group 2.272 to 2.090 Å (from {332} to {431} planes). The EDPs of the a-Li$_x$Si and c-Li$_{15}$Si$_4$ phases show some similarity in terms of *d*-spacing and intensity distribution, *i.e.*, the two diffuse bands from a-Li$_x$Si (Fig. 4j) overlap with the two groups of sharp rings from c-Li$_{15}$Si$_4$ (Fig. 5h). Numerous electrochemical studies have indicated a sudden crystallization of the a-Li$_x$Si to form c-Li$_{15}$Si$_4$,[36,58,60,107,108,120] which is consistent with our *in situ* TEM results of (1) structural similarity of the two phases; and (2) similar volume expansion (~300%) observed despite of whether a-Li$_x$Si or c-Li$_{15}$Si$_4$ is formed after lithiation. The identification of the c-Li$_{15}$Si$_4$ phase by electron diffraction is conclusive, while the detailed atomic structure of the a-Li$_x$Si phase requires further in-depth studies.[80,81] Based on these *in situ* studies, the maximum Li that can be alloyed with Si is 3.75 Li atoms per Si atom at room
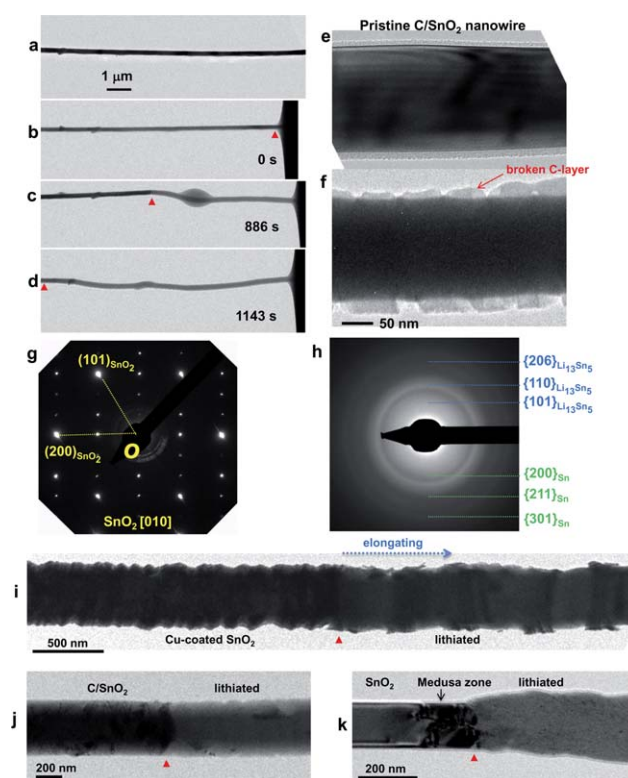

Fig. 6 Effect of a carbon coating layer on the lithiation behaviour of the SnO$_2$ nanowire. (a) Pristine C-coated SnO$_2$ nanowire. (b–d) Morphology evolution of the C-coated SnO$_2$ nanowire during lithiation. The red triangles mark the reaction fronts. (e–f) High magnification images showing the pristine C-coated SnO$_2$ nanowire with a continuous carbon coating layer on the nanowire surface (e), and the lithiated nanowire with broken and thickened carbon layer (f). No radial expansion was seen. (g–h) EDPs showing the phase transformation from a single crystalline SnO$_2$ (g) to an amorphous phase (h). (i) Suppression of radial expansion by Cu coating on a SnO$_2$ nanowire. The red triangle marks the position of the reaction front. Note the flat reaction frontis in contrast to the normally cusp-shaped reaction front of non-coated SnO$_2$ nanowire. (j-k) Effect of a coating layer on the morphology of the reaction front. With a coating layer, the reaction front was flat and no dislocation zone was seen (j), while it showed a cusp shape at the reaction front and high density dislocations without a coating layer (k). Reproduced with permission from the American Chemical Society.

Fig. 5 Fast and full lithiation of a P-doped and C-coated Si nanowire. (a) Pristine Si nanowire with a [112] growth direction. (b) Lithiated nanowire with a curved shape and without a c-Si core as seen in Fig. 4 for an intrinsic Si nanowire. (c) Delithiated nanowire. (d) EDP of the lithiated nanowire as shown in (b), showing the formation of the c-Li$_{15}$Si$_4$ phase. No diffraction spot from Si is seen, indicating a full lithiation. (e) EDP of the delithiated nanowire as shown in (c), showing a-Si structure. (f) High magnification image of the reaction front showing the core–shell lithiation manner and the c-Si to c-Li$_{15}$Si$_4$ transformation. (g) Statistics of improving lithiation rate and electrical conductivity by P-doping and C-coating. (h) Comparison of experimental and simulated EDPs from the c-Li$_{15}$Si$_4$ phase. Reproduced with permission from the American Chemical Society.

temperature, as such the room temperature capacity of Si should be 3579 mA h g^{-1}, consistent with recent electrochemical test results.[36,58,60,104,107,108]

3.4. Controlling lithiation-induced strain by coating

Lithiation induced strain and volume expansion are the killer of many high energy density anode materials, thus controlling lithiation induced strain through coating may improve the cyclability of many high energy density anode materials. Furthermore, conductive coatings are widely used in real batteries to enhance the rate and capacity performance,[102,116,121] as also demonstrated in C-coated Si nanowires,[80,112] but the microscopic mechanism of how the coating evolves during cycling is not clear. Using our *in situ* nano-battery setup, we have demonstrated alternation of the lithiation behaviour of the SnO$_2$ nanowires by applying a carbon, aluminium or copper (Cu) coating layer. As expected, a faster lithiation speed was seen for the coated SnO$_2$ nanowire than non-coated ones, and the same is true for Si nanowires.[83] More intriguingly, the coating layers suppressed the radial expansion, allowing only elongation during lithiation. Fig. 6 shows the lithiation of a C-coated SnO$_2$ nanowire. The nanowire showed a similar ESA process as seen for a non-coated nanowire (Fig. 6a–h), but without radial expansion (Fig. 6e–f). The carbon coating was thickened and broken after lithiation (Fig. 6f), indicating that the carbon layer also participated in lithiation. Fig. 6i shows the confining effect of an inert Cu coating on the SnO$_2$ nanowire. During lithiation, the nanowire elongated without radial swelling, and the Cu layer was stretched and broken after lithiation without thickening. More importantly, there was no dislocation or stress in the reaction front in all coated nanowires, indicating the enormously reduced strain by coating, which was in contrast to the non-coated

nanowires which always showed high density of dislocations in the reaction front.[79,83] We also noted that shape of the reaction front between the coated and non-coated nanowires was also different: namely the former show an almost flat reaction front (Fig. 6j),[83] while the latter always show a cusp shaped reaction front (Fig. 6k).[79] This difference is likely to be caused by the coating induced modification of Li$^+$ transport. In the lithiation of SnO$_2$ nanowires, there are two Li$^+$ transport paths: one *via* the thin surface ILE layer, and the other *via* the lithiated nanowire bulk. The coating is likely to affect the Li$^+$ transport *via* the surface ILE, slowing the Li$^+$ diffusion from the surface ILE layer to the nanowire bulk in the radial direction. These results demonstrated that the lithiation-induced strain can be intentionally controlled, and coating can not only enhance rate and capacity, but also modify lithiated induced strain, which may have important applications in implementing high energy density anode materials in LIBs.

We noted that most of the coating layers broke on the first lithiation cycle. However, because the biggest volume changes occur in the first lithiation process, and the volume changes in the later cycles are not significant, meaning that even the coating layer was broken after the first lithiation, it may still improve the cyclability significantly in the multiple cycles because of the overcoming of the electro-chemical shock in the first lithiation.

It should be noted that the suppression of radial expansion in Si nanowire was not observed, this is possibly because Si shows much larger radial expansion than that of SnO$_2$ nanowires, being 100% in the former and about 45% in the latter.

3.5. Li fibre growth on a nanowire anode

Li dendrite growth has been recognized as one of the major safety issues of the Li batteries using Li metal electrodes,[26,29,32,57,122] but
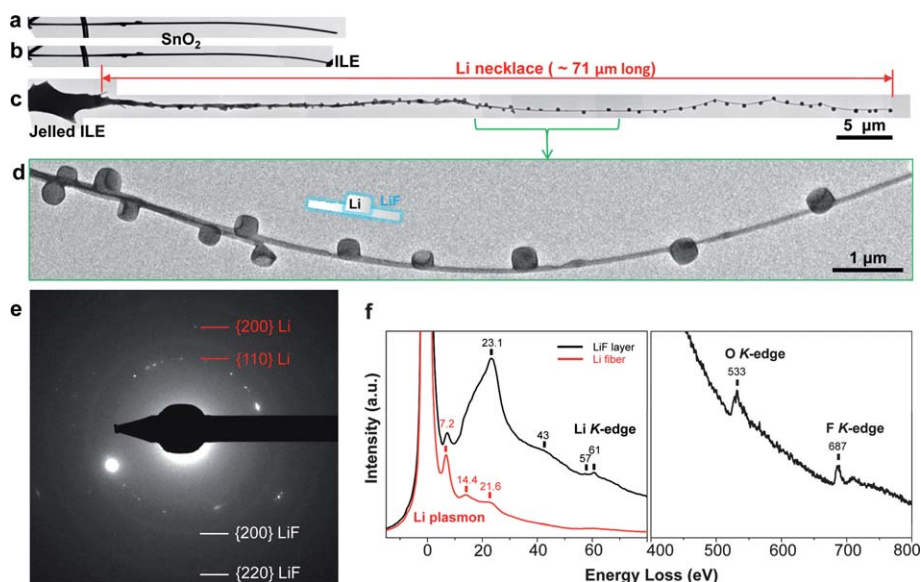

Fig. 7 Li fibre growth on the tip of a SnO$_2$ nanowire after lithiation. (a) Pristine SnO$_2$ nanowire. (b) The nanowire contacting the ILE. (c) Morphology of the immersed part after the ILE was retracted. The big chunk material on the left was jelled ILE, and the long Li necklace was about 71 μm long. (d) High magnification image showing a segment of the Li necklace. There were many Li crystals deposited on the thin and long Li stem. (e) EDP showing the sharp diffraction rings from multiple Li crystals and faint rings from tiny LiF crystallites. (f) EELS showing the plasmon peaks from Li crystals (red trace) and characteristic peaks from LiF layer (black trace; 23.1 eV in the low loss region and 687 eV from F *K*-edge).

not for conventional LIBs without reactive Li metal. However, ultra long Li fibres were found on the tip of a nanowire anode in the *in situ* charging tests in the liquid cell.[82]

Fig. 7 shows a 71 μm long Li "necklace" that was pulled out of the ILE after charging the SnO_2 nanowire. Both the EDP and EELS results confirmed that the necklace was made of a long Li fibre decorated with Li single crystals (Fig. 7d–f), which was covered by a thin layer of LiF. The Li fibre growth is attributed to the "tip effect", *i.e.*, an enhanced local electric field at the sharp nanowire tip inducing Li plating and electrolyte decomposition.[82] The Li fibre growth was found in different nanowire anodes, such as SnO_2 and Si, thus is general with the geometry rather than a specific material. LiF was not present in the original ILE, thus regarded as one of the products from electrolyte decomposition (fluorine is present in the –CF_3 group of the $TFSI^-$ anions).

The Li fibre growth is obviously caused by lithium plating, possibly because the lithiation potential applied in our experiments was close to that of Li.

The Li fibre is so long that it can cause a possible short circuit, since nanowire materials are regarded as increasingly popular candidates for next-generation LIBs. This *in situ* study brings up important safety precaution when using nanowire electrodes in a LIB.

3.6. Mechano-electrochemical coupling: anisotropic swelling of Si nanowire during lithiation

Anisotropic etching is known for Si,[123,124] interestingly, similar anisotropy was found in lithiated Si nanowires.[81,88] Fig. 8 shows the lithiation of a ⟨112⟩-oriented Si nanowire in the solid cell configuration. The pristine Si nanowire is straight and with uniform diameter (Fig. 8a), however, the lithiated part show unexpected
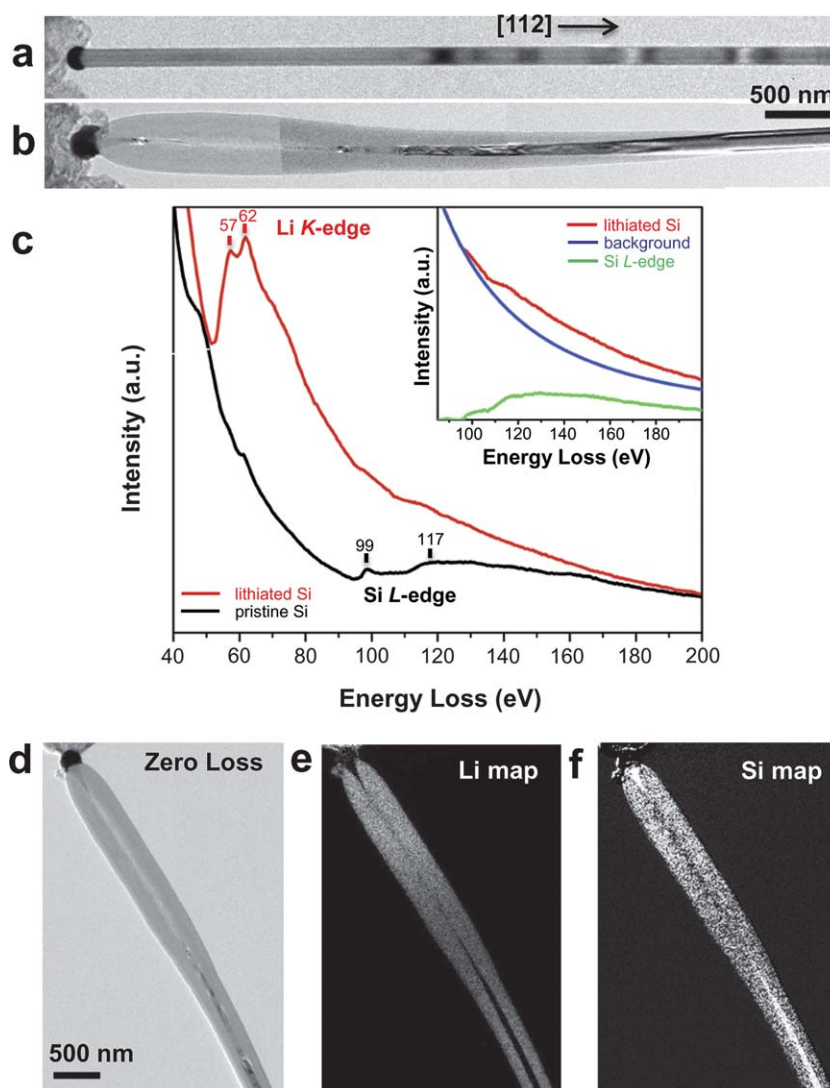

Fig. 8 Lithiation of a ⟨112⟩-oriented P-doped Si nanowire in the solid cell. (a) Pristine Si nanowire. (b) Partially lithiated Si nanowire showing huge volume expansion and tapered Si core. (c) EELS showing the onset of Li K-edge after lithiation (red trace) in contrast to the Si L-edge before lithiation (black trace). The inset spectrum shows the Si L-edge in the lithiated Si nanowire due to the diluted Si atoms in the $Li_{15}Si_4$ alloy. (d) Zero loss image. (e–f) Li and Si maps using Li K-edge (e) and Si L-edge (f), respectively. The centre of lithiated nanowire shows low intensity in the Li and Si maps (e–f) and high intensity in the zero loss image (d), indicating a thinner region or a crack. Reproduced with permission from the American Chemical Society.

morphology: (1) the radial expansion was extremely large; (2) the centre of the nanowire shows bright contrast rather than an expected dark contrast due to larger thickness. The EELS confirms lithium insertion, because the obvious Li K-edge ($\sim$60 eV) shows up while the intensity of the Si L-edge (100 to 140 eV) decreases (Fig. 8c). Less mass exists in the centre of the lithiated nanowire, as revealed by the bright contrast in the zero loss image (Fig. 8d), and the dark contrast in the Li and Si maps using the two well-separated Li K-edge and Si L-edge (Fig. 8e–f). The real shapes of Si nanowires before and after lithiation are better viewed by bending the wires and looking at the cross-section of the wires (Fig. 9). It is seen that the cylinder-shaped pristine Si nanowire (Fig. 9a) deformed to a widened dumbbell-shaped one after lithiation (Fig. 9b).

The crystallography of the anisotropic swelling is shown in the cross-sectional view in Fig. 9c. The axis of a pristine Si nanowire is along [112] direction, and there are two orthogonal directions on the cross-section, *i.e.*, [$1\bar{1}0$] and [$11\bar{1}$]. The Li insertion is much faster along the [$1\bar{1}0$] direction than the [$11\bar{1}$], leading to fast swelling along $\langle 110 \rangle$ because newly formed Li–Si alloy tends to expand to the opposite directions of the Li insertion. There is
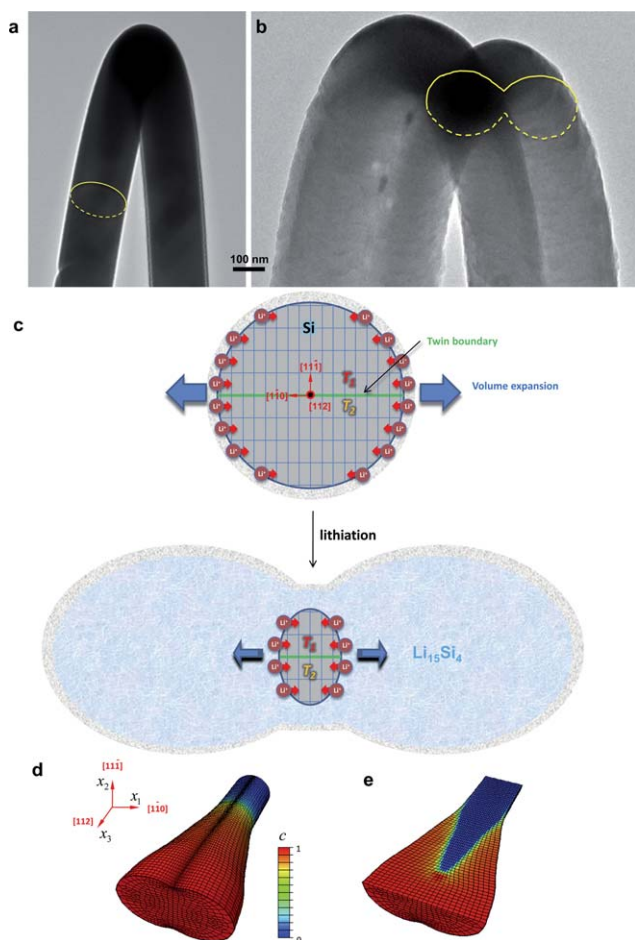
a twin boundary (TB) in the centre of the nanowire, separating the twins T_1 and T_2. During lithiation, T_1 and T_2 undergo anisotropic swelling independently. While the $\langle 112 \rangle$-oriented Si nanowires synthesized by the vapour–liquid–solid (VLS) mechanism usually have planar defects (TBs or stacking faults) parallel to the axis, they do not show detectable influence on the atomic lithiation mechanism of Si nanowires. The anisotropic swelling is also reproduced by finite element simulations (Fig. 9d and e), well capturing the dumbbell cross-section and the tapering c-Si core features. Qualitatively, the anisotropic expansion is induced by diffusion anisotropy and mechanical stress coupling effect: the diffusion along the $\langle 110 \rangle$ direction is slightly faster than that along the $\langle 111 \rangle$ direction, causing a slightly larger lithiation stress along the $\langle 110 \rangle$ direction than that along the $\langle 111 \rangle$ direction, and the larger stress enhances Li diffusion, meaning that Li diffusion along the $\langle 110 \rangle$ is accelerated once the lithiation was initiated. It is the coupling of diffusion anisotropy and lithiation induced mechanical stress that leads to the anisotropic volume expansion.[81]

Interestingly, similar anisotropic expansion was also observed in Si pillars.[125,126] The underlying mechanism for the anisotropic expansion should be similar to that in nanowires.

The anisotropic expansion raises the possibility of engineering the shape of Si nanowires or nano-pillars so that the volume expansion is occurring with the desired fashion. For instance, by designing the pitch distance and size of a $\langle 111 \rangle$-oriented Si pillar array may allow significant in-plane widening along the six $\langle 110 \rangle$ directions rather than out-of-plane elongation; by designing a $\langle 110 \rangle$-oriented Si pillar array may result in better adhesion to the substrate or current collector, because the volume changes are mostly along the out-of-plane pillar axes. Although nano-Si is expected to allow facile stress release, understanding of the detailed deformation manner will further enable rational design of the LIB electrodes so that the adverse mechanical effects can be minimized.

Fig. 9 Anisotropic swelling of a $\langle 112 \rangle$-oriented Si nanowire during lithiation. (a) Curved pristine Si nanowire with a cylinder shape. (b) Bent lithiated nanowire showing a dumbbell cross-section. (c) Crystallography of anisotropic swelling. (d–e) Finite element simulations showing the dumbbell cross-section (d) and the tapering c-Si core (e) during lithiation. Reproduced with permission from the American Chemical Society.

3.7. Size dependent fracture of Si nanoparticles during lithiation

Si nanoparticles are widely used to fabricate various Si-based anodes. Many efforts have been made to mitigate the fracture problem and to increase the capacity retention of Si electrodes. Although several studies have shown improved cyclability of the electrodes using nanometre-sized Si,[22,119] one of the fundamental issues remained unclear is: under what critical size a Si nanoparticle can be lithiated without cracking and fracture. Aiming at answering this question, we have conducted *in situ* lithiation experiments on individual Si nanoparticles with different sizes from several tens of nanometres up to several microns.[85]

Fig. 10 shows fracture of a large Si particle with a diameter of 540 nm when lithiated in the solid cell. The pristine Si particle had a round shape (Fig. 10a), which turned to be polyhedral during the lithiation process (Fig. 10b–f). The lithiation was also anisotropic, as some bumps were seen on certain facets (Fig. 10b–e), indicating preferential lithiation along these directions. When the lithiated shell was thickened to about 150 to 200 nm, some cracks were initiated from the particle surface (marked by the red arrowheads in Fig. 10e). These cracks developed and finally led to the fracture of the particle after full lithiation.

In sharp contrast to the crack and fracture of larger Si particles, smaller nanoparticles were lithiated without cracking
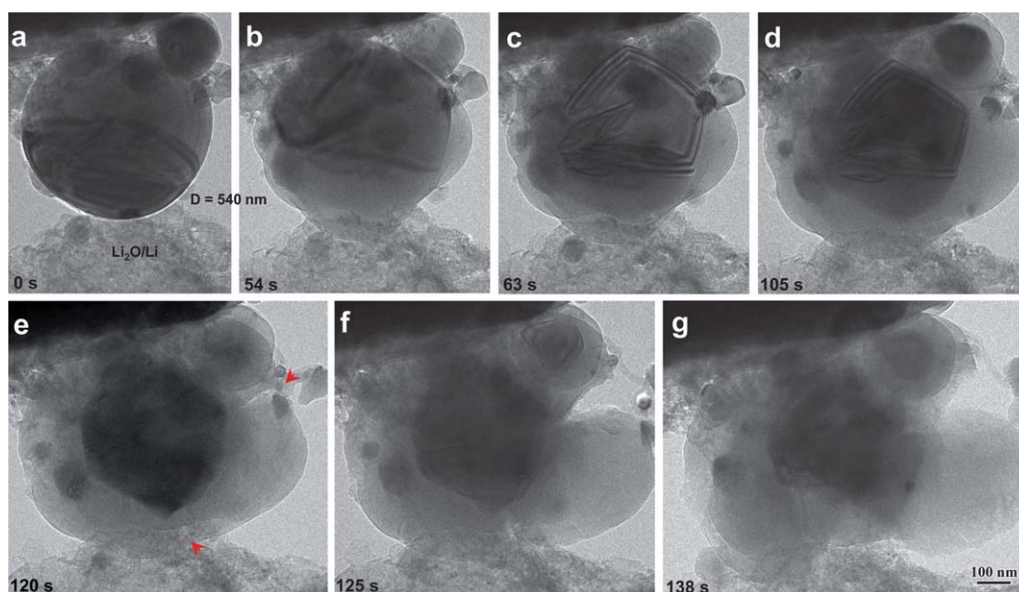
Fig. 10 Lithiation induced cracking and fracture of a big Si particle with a diameter of 540 nm. (a) Pristine Si particle in contact with the Li$_2$O/Li electrode. (b–d) Steady lithiation stage without cracking. The anisotropic lithiation resulted in a faceted Si core and some bumps in the Li$_x$Si shell with a light contrast. (e–g) Crack formation and fracture. When the Li$_x$Si shell is 150 to 200 nm thick, cracks were initiated from the particle surface (e), then developed (f) and finally broke the particle into pieces (g).

(Fig. 11). The larger Si particle ($D = 150$ nm) cracked upon full lithiation, while the smaller one ($d = 80$ nm) did not.

Our statistic studies showed that there exists a critical particle diameter of ∼150 nm, below which the particles neither cracked nor fractured upon lithiation, above which the particles first formed surface cracks and then fractured due to lithiation induced swelling. The unexpected surface fracture arose owing to the build-up of large tensile hoop stress in the surface layer that reversed the initial compression, and small-sized nanoparticles averted fracture because of insufficient mechanical energy to drive crack propagation during the electrochemical energy storage. These results provide direct evidence of the mechanical robustness of small silicon nanoparticles for their applications in lithium ion batteries, and are consistent with recent theoretical simulations showing plastic deformation during Si lithiation averting fracture failure.[127,128]
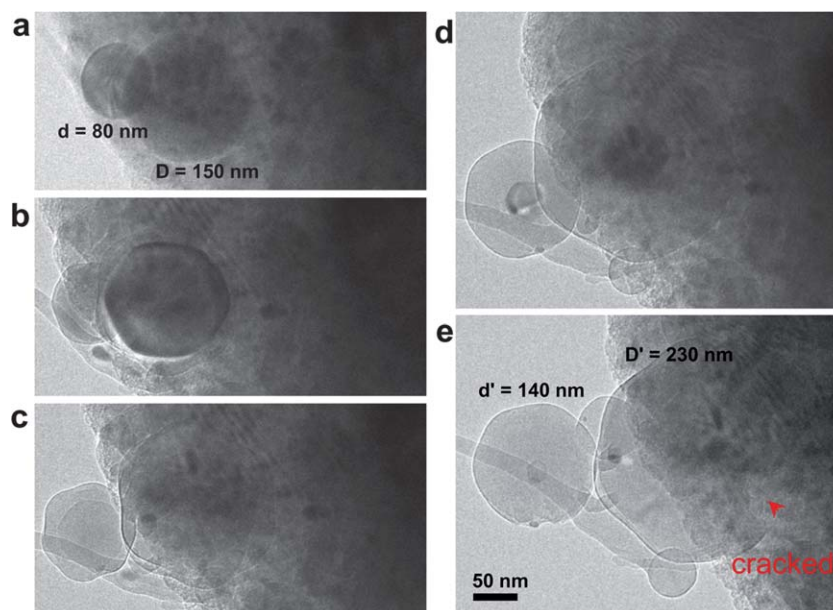

Fig. 11 Size dependent fracture of Si nanoparticles during lithiation. (a) Pristine Si nanoparticles with round shape. The smaller particle had a diameter of ∼80 nm and the big one ∼150 nm. (b–d) Lithiation process of the particles. The particles both showed core–shell structure, with hexagonal Si cores and bumps in the lithiated shell. (e) The larger particle cracked upon completion of lithiation, while the smaller particle remain integral when fully lithiated. Note that the final diameter of the smaller particle was about 140 nm, accounting for an expansion by 75% that was larger than the expected 56% expansion, probably due to the large swelling along the ⟨110⟩ direction when viewed along ⟨111⟩.

3.8. Solid electrolyte

All-solid batteries are currently attracting much attention because they require less packaging and safety measures than conventional LIBs using liquid electrolytes. Along this line, we have conducted some preliminary tests of SnO_2 nanowires or nanobelts coated with the solid-state LiAlSiO electrolyte by atomic layer deposition (ALD). Fig. 12a–l show the typical microstructure evolution of a LiAlSiO-coated SnO_2 nanobelt during lithiation. The nanobelt shows similar swelling, elongation, and crystalline to amorphous transformation to that of lithiated bare SnO_2 nanowires. Fig. 12m–p show a close view at the reaction front of another LiAlSiO-coated SnO_2 nanowire. It is seen that the LiAlSiO layer
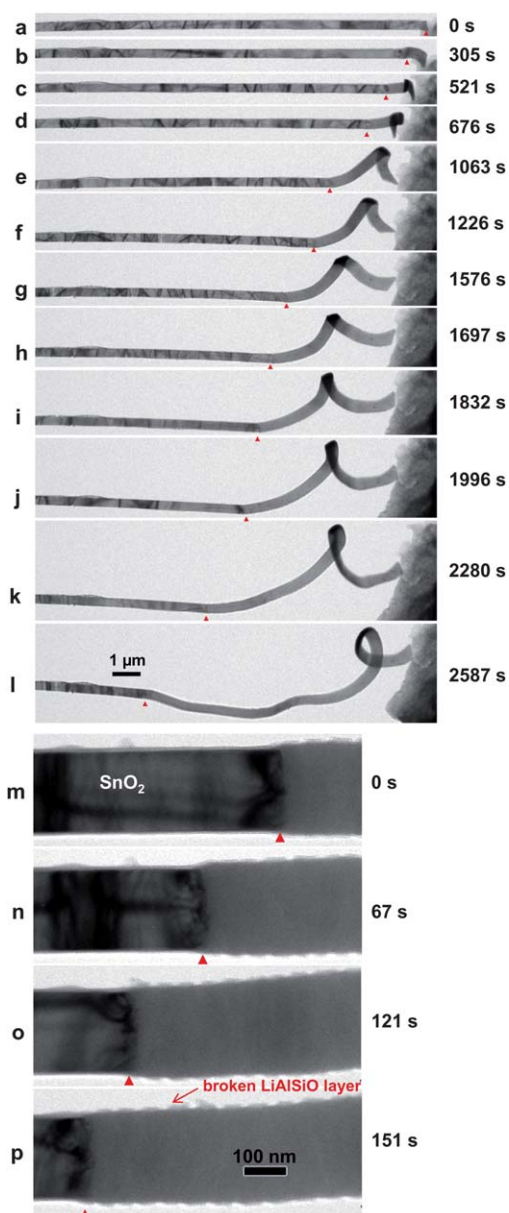
Fig. 12 Lithiation of SnO_2 nanobelts coated with the LiAlSiO solid-state electrolyte. (a–l) Overall morphology evolution viewed at a low magnification. (m–p) Close view of the reaction front during lithiation of another LiAlSiO-coated SnO_2 nanowire. The coating layer was broken after lithiation.

also broke when the reaction front swept over, similar to the case with carbon or metal coatings. These observations indicate that some buffer matrix may be necessary for the solid electrolyte when interfacing the anode material with large volume changes. The results also indicate that electrons can tunnel through the thin solid electrolyte layer easily.

4. Perspective

In situ TEM electrochemistry has been demonstrated as a powerful tool to probe the electrochemical reactions in real time, with high spatial resolution and possible concurrent structural and chemical analyses. It is expected that it will become an indispensable tool to advance mechanistic understanding of many electrochemical processes at the atomic scale. Using this nanobattery setup, one can "see" electron and ion transport in real time and at high spatial resolution. The tool can also be used to test new battery materials before they are implemented in LIBs for real industry applications. The nanobattery is not material limited, and can be used to test a wide range of electrode materials, such as lithium sulfur battery, and sodium sulfur battery. We can also use this tool to address some critical issues in LIBs, such as: what is the structure and formation mechanism of SEI? How does multiple cycling cause capacity fading and battery degradation and failure? We believe that *in situ* TEM electrochemistry can address the critical issues in LIBs, advance the science in LIBs, and lead to the development of advanced LIBs with high energy density, high power density and long cycle life time for applications in electrical vehicle and power back up for wind and solar energy.

However, *in situ* TEM electrochemistry is still in its infancy. Possible directions to improve this technique and to make it even more powerful are provided in the following.

4.1. Find the missing current

In our experiments, the lithiation/delithiation tests were conducted by potentiostatic hold, *i.e.*, by applying a constant potential over the cell, because the current was too small to measure (estimated to be in the femtoampere (fA) range for a single nanowire less than 200 nm in diameter and about 10 μm in length) due to the finite mass involved. Although variation of potential control, such as a staircase-like potential, or the use of large amount of active materials could be applied, controlling the small current on the femtoampere (fA) level is highly demanded.

A considerable portion of the conventional electrochemical tests are conducted with current control, including sourcing and measuring, such as galvanostatic charging/discharging, cyclic voltammetry, *etc.* To correlate the high spatial resolution dynamic microstructure evolution with key electrochemical signal such as the charging current and potential, the "missing" current should be retrieved in an improved instrumentation.

The problem is possibly beyond just using a better amperemeter. Nanomaterials are known to have more predominant surface/interface phenomena due to the high specific surface area, which may behave quite differently from their bulk counterparts.[13,129] For instance, we have seen the large amount of

jelled electrolyte on a C-coated sample or long Li fibres grown on the nanowire tips,[80] implying that the interface or side reactions may contribute significantly to the measured current. Fortunately, with *in situ* TEM, morphology observation and structural analysis can offer a backup to supplement the measured curves. Once the delicate current control is at place, a direct link between the microstructure change and the electrochemical parameters can be made, such as the causes for irreversible capacity loss, changes in columbic efficiency, *etc.*

4.2. *In situ* studies of cathode materials and SEI

Currently, cathode materials of LIBs show lower capacity and kinetics than the anode materials, which limit the energy and power density of LIBs.[104] A cathode material usually shows less dramatic change in volume and structure during cycling than an anode material, thus is hard to characterize by some techniques, such as *in situ* optical microscopy. *In situ* TEM is particularly suitable for studying the cathode materials to reveal the subtle structural changes during the electrochemical reactions. It is expected that this technique will play an important role in unfolding the phase transformation mechanism and high resolution structural evolution of cathode materials in LIBs during cycling.

SEI formation affects the electrochemical reaction kinetics, the cycle lifetime, and the overall performance of LIBs. Understanding the formation mechanism and the microstructure of SEI has attracted much attention but little details (structure, composition, kinetics, *etc.*) are known. The nanobattery setup that we created can potentially provide atomic scale dynamic information about how SEI is formed, and how does it evolve, thus provide critical information on how to optimize the SEI layer to improve the performance of LIBs.

4.3. *In situ* electrochemical corrosion, plating, electrolysis, and nanoparticles growth

Many physical or chemical processes, such as electrochemical plating, corrosion, electrolysis, and nanoparticle growth, *etc.*, involve the usage of liquid phases. With the current experimental setups, the methodology can be readily extended to these other related fields. In fact, in our experiments, we observed electrochemical corrosion of nanowires, and electrochemical plating of materials on the nanowire surface (Fig. 13). In Fig. 13a, the etching of the nanowire occurred in a segment covered by a bead, and because of the small size of the bead, the entire etching process can be followed. The etching was probably caused by the HF due to decomposition of the electrolyte. Similarly, in Fig. 13d and e, the Au nanoparticle on the Si nanowire tip was etched
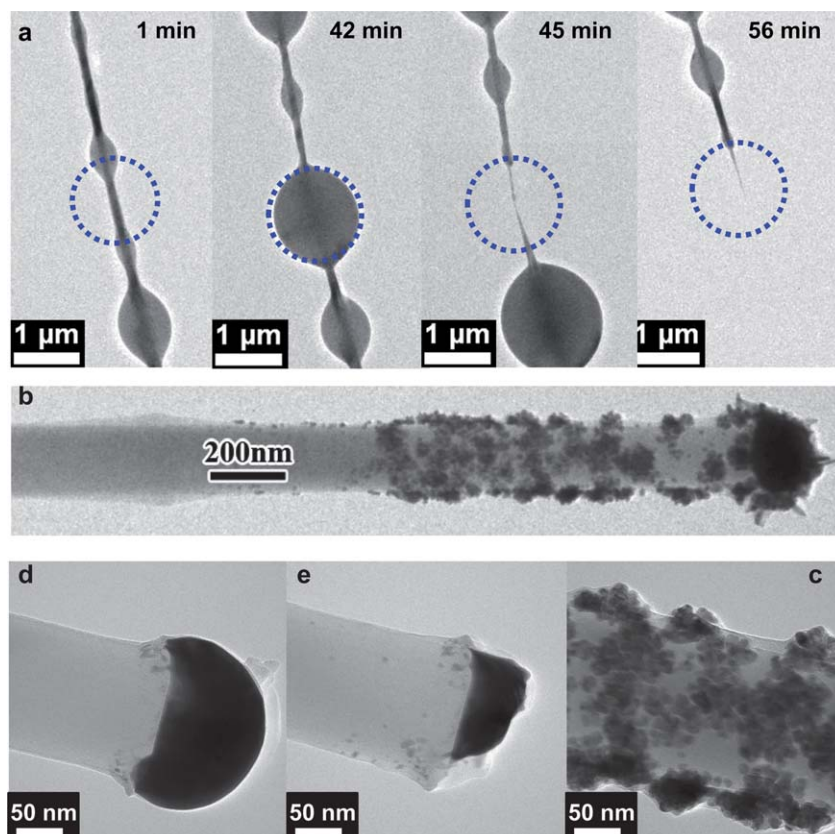

Fig. 13 *In situ* etching and plating observed in an ILE cell. (a) Electrochemical etching of SnO_2 nanowires. The nanowire was biased at -4 V with respect to the $LiCoO_2$ cathode in an ILE cell. The etching is possibly caused by the ILE decomposition, forming HF that etched the nanowire. (b–c) Electrochemical plating of Ag nanoparticles on the surface of a Si nanowire. Biasing condition is the same as (a), but the ILE covered the Ag paste used to glue the $LiCoO_2$ to an Al rod. (d–e) Etching an Au particle on the tip of the Si nanowire. Biasing condition is the same as the SnO_2 nanowire shown in (a).

away partly. Fig. 13b and c show the plating of Ag nanoparticles on the surface of Si nanowires. This was caused by accidental coverage of the ILE with the silver epoxy on the cathode side. These preliminary experiments point to very promising applications of our technique in a broad electrochemical field.

4.4. Multiple-probe multiple function platform for *in situ* probing of LIBs

Although the current nanobattery allows for real time dynamic studies of LIBs, the follow up real time studies of the electrical, mechanical properties of the lithiated product are still difficult. This kind of study is important, as the lithiated materials show dramatic different electrical, mechanical, and other physical properties as compared to the pristine non-lithiated materials. Postmortem studies of the lithiated materials are usually very difficult because they are very sensitive to air. In this context, we propose to implement a multiple-probe multiple functional platform based on our nanobattery setup to enable immediate electrical and mechanical probing of the lithiated product by *in situ* TEM. As previously mentioned, the open-cell design allows large room for manipulation, measurement, and characterization of the cycled material. With the piezo-positioner in use, one can put multiple probes such as STM, and atomic force microscopy (AFM) probes onto the same platform to enable multiple functional probing. For instance, some possible functions can be added to the current configurations:

(1) Electrical measurement: probes can be mounted to measure the conductivity change before and after lithiation;

(2) Mechanical measurements: AFM cantilevers can be added for *in situ* mechanical property measurement of the materials before and after lithiation;

(3) *In situ* electrolyte dispersion: a thin layer of electrolyte may be fetched from the electrolyte reservoir by one nanowire. Then the anode/electrolyte/cathode couple can be made to allow visualization of the whole battery.

The essence of these designs is to gather as much information as possible from the *same individual* sample, so that a complete understanding of the nanoscale electrochemistry becomes possible.

5. Conclusions

In summary, the power of using the *in situ* transmission electron microscopy to study electrochemistry includes (1) high spatial resolution down to atomic scale; (2) dynamic observation of whole cycling process; (3) full structural and chemical characterization; and (4) *in situ* manipulation and probing the cycled materials. Examples of various anode materials studied with this technique are given, in general showing material specific electrochemical behaviours. The discussion in this review has illustrated the great promise of studying electrochemistry with *in situ* transmission electron microscopy, but there is plenty of room for improvement and seamless connection to the conventional electrochemistry: (1) controlling the current to trigger a designed electrochemical process to occur thus coupling the structural and electrochemical characterizations of the same sample under test; (2) studying cathode materials and SEI layers with subtle changes in the electrochemical processes; (3) incorporation of

more characterization and manipulation tools onto the platform to retrieve more information from an individual sample; and (4) extending the technique to fields beyond batteries.

Notes and references

1 B. Kang and G. Ceder, *Nature*, 2009, **458**, 190–193.
2 J. B. Goodenough and Y. Kim, *Chem. Mater.*, 2010, **22**, 587–603.
3 J. T. Han, Y. H. Huang and J. B. Goodenough, *Chem. Mater.*, 2011, **23**, 2027–2029.
4 Y. Shao-Horn, L. Croguennec, C. Delmas, E. C. Nelson and M. A. O'Keefe, *Nat. Mater.*, 2003, **2**, 464–467.
5 S. Y. Chung, J. T. Bloking and Y. M. Chiang, *Nat. Mater.*, 2002, **1**, 123–128.
6 J. M. Tarascon and M. Armand, *Nature*, 2001, **414**, 359–367.
7 L. Ji, Z. Lin, M. Alcoutlabi and X. Zhang, *Energy Environ. Sci.*, 2011, **4**, 2682–2699.
8 F. F. Cao, Y. G. Guo and L. J. Wan, *Energy Environ. Sci.*, 2011, **4**, 1634–1642.
9 D. Deng, M. G. Kim, J. Y. Lee and J. Cho, *Energy Environ. Sci.*, 2009, **2**, 818–837.
10 D. W. Liu and G. Z. Cao, *Energy Environ. Sci.*, 2010, **3**, 1218–1237.
11 V. G. Pol and M. M. Thackeray, *Energy Environ. Sci.*, 2011, **4**, 1904–1912.
12 Z. S. Hong, X. Z. Zheng, X. K. Ding, L. L. Jiang, M. D. Wei and K. M. Wei, *Energy Environ. Sci.*, 2011, **4**, 1886–1891.

13 X. H. Liu, Y. J. Lin, S. Zhou, S. Sheehan and D. W. Wang, *Energies*, 2010, **3**, 285–300.

14 Y. Hamon, T. Brousse, F. Jousse, P. Topart, P. Buvat and D. M. Schleich, *J. Power Sources*, 2001, **97–98**, 185–187.

15 Q. F. Li and N. J. Bjerrum, *J. Power Sources*, 2002, **110**, 1–10.

16 S. C. Chao, Y. C. Yen, Y. F. Song, Y. M. Chen, H. C. Wu and N. L. Wu, *Electrochem. Commun.*, 2010, **12**, 234–237.

17 L. Baggetto and P. H. L. Notten, *J. Electrochem. Soc.*, 2009, **156**, A169–A175.

18 L. Baggetto, E. J. M. Hensen and P. H. L. Notten, *Electrochim. Acta*, 2010, **55**, 7074–7079.

19 P. Limthongkul, Y. I. Jang, N. J. Dudney and Y. M. Chiang, *Acta Mater.*, 2003, **51**, 1103–1113.

20 H. Li, X. J. Huang, L. Q. Chen, G. W. Zhou, Z. Zhang, D. P. Yu, Y. J. Mo and N. Pei, *Solid State Ionics*, 2000, **135**, 181–191.

21 J. Li and J. R. Dahn, *J. Electrochem. Soc.*, 2007, **154**, A156–A161.

22 C. K. Chan, H. L. Peng, G. Liu, K. McIlwrath, X. F. Zhang, R. A. Huggins and Y. Cui, *Nat. Nanotechnol.*, 2008, **3**, 31–35.

23 J. R. Szczech and S. Jin, *Energy Environ. Sci.*, 2011, **4**, 56–72.

24 D. Larcher, S. Beattie, M. Morcrette, K. Edstroem, J. C. Jumas and J. M. Tarascon, *J. Mater. Chem.*, 2007, **17**, 3759–3772.

25 M. Arakawa, S. Tobishima, Y. Nemoto, M. Ichimura and J. Yamaki, *J. Power Sources*, 1993, **43**, 27–35.

26 M. Rosso, C. Brissot, A. Teyssot, M. Dolle, L. Sannier, J. M. Tarascon, R. Bouchetc and S. Lascaud, *Electrochim. Acta*, 2006, **51**, 5334–5340.

27 D. Chen, S. Indris, M. Schulz, B. Gamer and R. Mönig, *J. Power Sources*, 2011, **196**, 6382–6387.

28 P. R. Raimann, N. S. Hochgatterer, C. Korepp, K. C. Moller, M. Winter, H. Schrottner, F. Hofer and J. O. Besenhard, *Ionics*, 2006, **12**, 253–255.

29 F. Orsini, A. Du Pasquier, B. Beaudoin, J. M. Tarascon, M. Trentin, N. Langenhuizen, E. De Beer and P. Notten, *J. Power Sources*, 1998, **76**, 19–29.

30 F. Orsini, A. du Pasquier, B. Beaudouin, J. M. Tarascon, M. Trentin, N. Langenhuizen, E. de Beer and P. Notten, *J. Power Sources*, 1999, **81**, 918–921.

31 P. Baudry, M. Armand, M. Gauthier and J. Masounave, *Solid State Ionics*, 1988, **28**, 1567–1571.

32 M. Dolle, L. Sannier, B. Beaudoin, M. Trentin and J. M. Tarascon, *Electrochem. Solid-State Lett.*, 2002, **5**, A286–A289.

33 M. Balasubramanian, X. Sun, X. Q. Yang and J. McBreen, *J. Power Sources*, 2001, **92**, 1–8.

34 X. Q. Yang, J. McBreen, W. S. Yoon and C. P. Grey, *Electrochem. Commun.*, 2002, **4**, 649–654.

35 X. Q. Yang, J. McBreen, W. S. Yoon, M. Yoshio, H. Y. Wang, K. Fukuda and T. Umeno, *Electrochem. Commun.*, 2002, **4**, 893–897.

36 T. D. Hatchard and J. R. Dahn, *J. Electrochem. Soc.*, 2004, **151**, A838–A842.

37 X.-J. Wang, H.-Y. Chen, X. Yu, L. Wu, K.-W. Nam, J. Bai, H. Li, X. Huang and X.-Q. Yang, *Chem. Commun.*, 2011, **47**, 7170–7172.

38 J. R. Dahn and R. R. Haering, *Solid State Commun.*, 1981, **40**, 245–248.

39 J. M. Tarascon, A. S. Gozdz, C. Schmutz, F. Shokoohi and P. C. Warren, *Solid State Ionics*, 1996, **86–88**, 49–54.

40 S. Patoux, G. Rousse, J.-B. Leriche and C. Masquelier, *Chem. Mater.*, 2003, **15**, 2084–2093.

41 C. Baehtz, T. Buhrmester, N. N. Bramnik, K. Nikolowski and H. Ehrenberg, *Solid State Ionics*, 2005, **176**, 1647–1652.

42 J. B. Leriche, S. Hamelet, J. Shu, M. Morcrette, C. Masquelier, G. Ouvrard, M. Zerrouki, P. Soudan, S. Belin, E. Elkaim and F. Baudelet, *J. Electrochem. Soc.*, 2010, **157**, A606–A610.

43 N. K. Karan, D. P. Abraham, M. Balasubramanian, M. M. Furczon, R. Thomas and R. S. Katiyar, *J. Electrochem. Soc.*, 2009, **156**, A553–A562.

44 I. Nakai and T. Nakagome, *Electrochem. Solid-State Lett.*, 1998, **1**, 259–261.

45 O. Haas, A. Deb, E. J. Cairns and A. Wokaun, *J. Electrochem. Soc.*, 2005, **152**, A191–A196.

46 A. Deb, U. Bergmann, E. J. Cairns and S. P. Cramer, *J. Synchrotron Radiat.*, 2004, **11**, 497–504.

47 F. Kong, R. Kostecki, G. Nadeau, X. Song, K. Zaghib, K. Kinoshita and F. McLarnon, *J. Power Sources*, 2001, **97–98**, 58–66.

48 L. J. Hardwick, P. W. Ruch, M. Hahn, W. Scheifele, R. Kotz and P. Novak, *J. Phys. Chem. Solids*, 2008, **69**, 1232–1237.

49 J. T. Li, J. C. Fang, H. Su and S. G. Sun, *Progr. Chem.*, 2011, **23**, 349–356.

50 A. Wuersig, W. Scheifele and P. Novak, *J. Electrochem. Soc.*, 2007, **154**, A449–A454.

51 G. Gachot, P. Ribiere, D. Mathiron, S. Grugeon, M. Armand, J. B. Leriche, S. Pilard and S. Laruelle, *Anal. Chem.*, 2011, **83**, 478–485.

52 T. Doi, L. Zhao, M. Zhou, S. Okada and J. Yamaki, *J. Power Sources*, 2008, **185**, 1380–1385.

53 S. H. Lee, J. M. Jung, J. H. Ok and C. H. Park, *J. Power Sources*, 2010, **195**, 5049–5051.

54 I. Watanabe and J. Yamaki, *J. Power Sources*, 2006, **153**, 402–404.

55 L. W. Zhao, I. Watanabe, T. Doi, S. Okada and J. Yamaki, *J. Power Sources*, 2006, **161**, 1275–1280.

56 A. R. Armstrong, M. Holzapfel, P. Novak, C. S. Johnson, S. H. Kang, M. M. Thackeray and P. G. Bruce, *J. Am. Chem. Soc.*, 2006, **128**, 8694–8698.

57 R. Bhattacharyya, B. Key, H. L. Chen, A. S. Best, A. F. Hollenkamp and C. P. Grey, *Nat. Mater.*, 2010, **9**, 504–510.

58 B. Key, R. Bhattacharyya, M. Morcrette, V. Seznec, J. M. Tarascon and C. P. Grey, *J. Am. Chem. Soc.*, 2009, **131**, 9239–9249.

59 M. Letellier, F. Chevallier, C. Clinard, E. Frackowiak, J.-N. Rouzaud, F. Beguin, M. Morcrette and J.-M. Tarascon, *J. Chem. Phys.*, 2003, **118**, 6038–6045.

60 B. Key, M. Morcrette, J. M. Tarascon and C. P. Grey, *J. Am. Chem. Soc.*, 2011, **133**, 503–512.

61 N. Balke, S. Jesse, A. N. Morozovska, E. Eliseev, D. W. Chung, Y. Kim, L. Adamczyk, R. E. Garcia, N. Dudney and S. V. Kalinin, *Nat. Nanotechnol.*, 2010, **5**, 749–754.

62 Y. Tian, A. Timmons and J. R. Dahn, *J. Electrochem. Soc.*, 2009, **156**, A187–A191.

63 M. Inaba, Y. Kawatate, A. Funabiki, S. K. Jeong, T. Abe and Z. Ogumi, *Electrochim. Acta*, 1999, **45**, 99–105.

64 M. Inaba, T. Doi, Y. Iriyama, T. Abe and Z. Ogumi, *J. Power Sources*, 1999, **81**, 554–557.

65 R. Sharma, P. A. Crozier and M. M. J. Treacy, *NSF Workshop Report on Dynamic* In situ *Electron Microscopy as a Tool to Meet the Challenges of the Nanoworld*, Tempe, 2006.

66 C. H. Jin, K. Suenaga and S. Iijima, *Nat. Nanotechnol.*, 2008, **3**, 17–21.

67 D. S. Shih, I. M. Robertson and H. K. Birnbaum, *Acta Metall.*, 1988, **36**, 111–124.

68 M. Legros, M. Cabie and D. S. Gianola, *Microsc. Res. Tech.*, 2009, **72**, 270–283.

69 M. L. Taheri, T. Lagrange, B. W. Reed, M. R. Armstrong, G. H. Campbell, W. J. DeHope, J. S. Kim, W. E. King, D. J. Masiel and N. D. Browning, *Microsc. Res. Tech.*, 2009, **72**, 122–130.

70 R. Sharma, *Microsc. Res. Tech.*, 2009, **72**, 144–152.

71 S. Kodambaka, J. Tersoff, M. C. Reuter and F. M. Ross, *Science*, 2007, **316**, 729–732.

72 J. B. Hannon, S. Kodambaka, F. M. Ross and R. M. Tromp, *Nature*, 2006, **440**, 69–71.

73 Z. W. Shan, R. K. Mishra, S. A. S. Asif, O. L. Warren and A. M. Minor, *Nat. Mater.*, 2008, **7**, 115–119.

74 H. Zheng, A. J. Cao, C. R. Weinberger, J. Y. Huang, K. Du, J. B. Wang, Y. Y. Ma, Y. N. Xia and S. X. Mao, *Nat. Prod. Commun.*, 2010, **1**, 144.

75 Y. Lu, J. Y. Huang, C. Wang, S. H. Sun and J. Lou, *Nat. Nanotechnol.*, 2010, **5**, 218–224.

76 J. Y. Huang, S. Chen, Z. Q. Wang, K. Kempa, Y. M. Wang, S. H. Jo, G. Chen, M. S. Dresselhaus and Z. F. Ren, *Nature*, 2006, **439**, 281.

77 J. Y. Huang, S. Chen, S. H. Jo, Z. Wang, D. X. Han, G. Chen, M. S. Dresselhaus and Z. F. Ren, *Phys. Rev. Lett.*, 2005, **94**, 236802.

78 X. H. Liu, J. Zhu, C. H. Jin, L. M. Peng, D. M. Tang and H. M. Cheng, *Nanotechnology*, 2008, **19**, 085711.

79 J. Y. Huang, L. Zhong, C. M. Wang, J. P. Sullivan, W. Xu, L. Q. Zhang, S. X. Mao, N. S. Hudak, X. H. Liu, A. Subramanian, H. Y. Fan, L. Qi, A. Kushima and J. Li, *Science*, 2010, **330**, 1515–1520.

80 X. H. Liu, L. Q. Zhang, L. Zhong, Y. Liu, H. Zheng, J. W. Wang, J.-H. Cho, S. A. Dayeh, S. T. Picraux, J. P. Sullivan, S. X. Mao, Z. Z. Ye and J. Y. Huang, *Nano Lett.*, 2011, **11**, 2251–2258.

81 X. H. Liu, H. Zheng, L. Zhong, S. Huang, K. Karki, L. Q. Zhang, Y. Liu, A. Kushima, W. T. Liang, J. W. Wang, J.-H. Cho,

This journal is © The Royal Society of Chemistry 2011

Energy Environ. Sci., 2011, **4**, 3844–3860 | 3859

E. Epstein, S. T. Picraux, T. Zhu, J. Li, J. P. Sullivan, J. Cumings, C. Wang, S. X. Mao, Z. Z. Ye, S. Zhang and J. Y. Huang, *Nano Lett.*, 2011, DOI: 10.1021/nl201684d.

82 X. H. Liu, L. Zhong, L. Q. Zhang, A. Kushima, S. X. Mao, J. Li, Z. Z. Ye, J. P. Sullivan and J. Y. Huang, *Appl. Phys. Lett.*, 2011, **98**, 183107.

83 L. Q. Zhang, X. H. Liu, Y. Liu, S. Huang, T. Zhu, L. Gui, S. X. Mao, Z. Z. Ye, C. M. Wang, J. P. Sullivan and J. Y. Huang, *ACS Nano*, 2011, **5**, 4800–4809.

84 L. Zhong, X. H. Liu, C. M. Wang, G. F. Wang, S. X. Mao and J. Y. Huang, *Phys. Rev. Lett.*, 2011, **106**, 248302.

85 X. H. Liu, L. Zhong, S. Huang, S. X. Mao, T. Zhu and J. Y. Huang, 2011, submitted.

86 C.-M. Wang, W. Xu, J. Liu, J.-G. Zhang, L. V. Saraf, B. W. Arey, D. Choi, Z.-G. Yang, J. Xiao, S. Thevuthasan and D. R. Baer, *Nano Lett.*, 2011, **11**, 1874–1880.

87 C. M. Wang, W. Xu, J. Liu, D. W. Choi, B. Arey, L. V. Saraf, J. G. Zhang, Z. G. Yang, S. Thevuthasan, D. R. Baer and N. Salmon, *J. Mater. Res.*, 2010, **25**, 1541–1547.

88 X. H. Liu, H. Zheng, L. Zhong, S. Huang, K. Karki, L. Q. Zhang, Y. Liu, A. Kushima, W. T. Liang, J. W. Wang, J.-H. Cho, E. Epstein, S. T. Picraux, T. Zhu, J. Li, J. P. Sullivan, J. Cumings, C. Wang, S. X. Mao, S. Zhang and J. Y. Huang, *Anisotropic Volume Expansion and Ultrafast Lithiation of Si Nanowires Revealed by* In-situ *Transmission Electron Microscopy*, Annapolis, Maryland, May 31–June 2, 2011.

89 N. de Jonge, D. B. Peckys, G. J. Kremers and D. W. Piston, *Proc. Natl. Acad. Sci. U. S. A.*, 2009, **106**, 2159–2164.

90 J. P. Sullivan, J. Huang, M. J. Shaw, A. Subramanian, N. Hudak, Y. Zhan and J. Lou, *Energy Harvesting and Storage: Materials, Devices, and Applications*, 2010, p. 7683.

91 H. M. Zheng, R. K. Smith, Y. W. Jun, C. Kisielowski, U. Dahmen and A. P. Alivisatos, *Science*, 2009, **324**, 1309–1312.

92 M. J. Williamson, R. M. Tromp, P. M. Vereecken, R. Hull and F. M. Ross, *Nat. Mater.*, 2003, **2**, 532–536.

93 A. Brazier, L. Dupont, L. Dantras-Laffont, N. Kuwata, J. Kawamura and J. M. Tarascon, *Chem. Mater.*, 2008, **20**, 2352–2359.

94 K. Yamamoto, Y. Iriyama, T. Asaka, T. Hirayama, H. Fujita, C. A. J. Fisher, K. Nonaka, Y. Sugita and Z. Ogumi, *Angew. Chem., Int. Ed.*, 2010, **49**, 4414–4417.

95 D. R. MacFarlane, P. Meakin, J. Sun, N. Amini and M. Forsyth, *J. Phys. Chem. B*, 1999, **103**, 4164–4170.

96 M. Galinski, A. Lewandowski and I. Stepniak, *Electrochim. Acta*, 2006, **51**, 5567–5580.

97 Sciencelab Website, http://www.sciencelab.com/msdsList.php, accessed May 23, 2011.

98 K. Svensson, Y. Jompol, H. Olin and E. Olsson, *Rev. Sci. Instrum.*, 2003, **74**, 4945–4947.

99 M. M. Islam, T. Bredow and C. Minot, *J. Phys. Chem. B*, 2006, **110**, 9413–9420.

100 D. R. Liu and D. B. Williams, *Philos. Mag. B*, 1986, **53**, L123–L128.

101 P. Vajda and F. Beuneu, *Phys. Rev. B: Condens. Matter*, 1996, **53**, 5335–5340.

102 N. H. Zhao, L. C. Yang, P. Zhang, G. J. Wang, B. Wang, B. D. Yao and Y. P. Wu, *Mater. Lett.*, 2010, **64**, 972–975.

103 H. Qiao, Z. Zheng, L. Z. Zhang and L. F. Xiao, *J. Mater. Sci.*, 2008, **43**, 2778–2784.

104 U. Kasavajjula, C. S. Wang and A. J. Appleby, *J. Power Sources*, 2007, **163**, 1003–1039.

105 P. Limthongkul, Y. I. Jang, N. J. Dudney and Y. M. Chiang, *J. Power Sources*, 2003, **119**, 604–609.

106 R. Nesper and H. G. Vonschnering, *J. Solid State Chem.*, 1987, **70**, 48–57.

107 M. N. Obrovac and L. Christensen, *Electrochem. Solid-State Lett.*, 2004, **7**, A93–A96.

108 M. N. Obrovac and L. J. Krause, *J. Electrochem. Soc.*, 2007, **154**, A103–A108.

109 L. Y. Beaulieu, K. W. Eberman, R. L. Turner, L. J. Krause and J. R. Dahn, *Electrochem. Solid-State Lett.*, 2001, **4**, A137–A140.

110 Z. H. Chen, L. Christensen and J. R. Dahn, *Electrochem. Commun.*, 2003, **5**, 919–923.

111 N. Ravet, A. Abouimrane and M. Armand, *Nat. Mater.*, 2003, **2**, 702.

112 R. Huang, X. Fan, W. C. Shen and J. Zhu, *Appl. Phys. Lett.*, 2009, **95**, 133119.

113 T. Ishihara, M. Nakasu, M. Yoshio, H. Nishiguchi and Y. Takita, *J. Power Sources*, 2005, **146**, 161–165.

114 M. H. Kong, D. J. Byun and J. K. Lee, in *Advanced Materials and Processing*, ed. D. J. Byun, J. K. Kim and C. S. Lee, 2007, vol. 26–28, pp. 333–336.

115 L. F. Cui, Y. Yang, C. M. Hsu and Y. Cui, *Nano Lett.*, 2009, **9**, 3370–3374.

116 S. H. Ng, J. Z. Wang, D. Wexler, K. Konstantinov, Z. P. Guo and H. K. Liu, *Angew. Chem., Int. Ed.*, 2006, **45**, 6896–6899.

117 S. Zhou, X. H. Liu and D. W. Wang, *Nano Lett.*, 2010, **10**, 860–863.

118 K. S. Park, J. G. Kang, Y. J. Choi, S. Lee, D. W. Kim and J. G. Park, *Energy Environ. Sci.*, 2011, **4**, 1796–1801.

119 A. Magasinski, P. Dixon, B. Hertzberg, A. Kvit, J. Ayala and G. Yushin, *Nat. Mater.*, 2010, **9**, 461.

120 L. Baggetto, R. A. H. Niessen, F. Roozeboom and P. H. L. Notten, *Adv. Funct. Mater.*, 2008, **18**, 1057–1066.

121 X. X. Ji, X. T. Huang, J. P. Liu, J. Jiang, X. Li, R. M. Ding, Y. Y. Hu, F. Wu and Q. Li, *Nanoscale Res. Lett.*, 2010, **5**, 649–653.

122 S. Tobishima, Y. Sakurai and J. Yamaki, *J. Power Sources*, 1997, **68**, 455–458.

123 H. Seidel, L. Csepregi, A. Heuberger and H. Baumgartel, *J. Electrochem. Soc.*, 1990, **137**, 3612–3626.

124 B. Q. Wu, A. Kumar and S. Pamarthy, *J. Appl. Phys.*, 2010, **108**, 051101.

125 J. L. Goldman, B. R. Long, A. A. Gewirth and R. G. Nuzzo, *Adv. Funct. Mater.*, 2011, **21**, 2412–2422.

126 S. W. Lee, M. T. McDowell, J. W. Choi and Y. Cui, *Nano Lett.*, 2011, **11**, 3034–3039.

127 K. J. Zhao, M. Pharr, J. J. Vlassak and Z. G. Suo, *J. Appl. Phys.*, 2011, **109**, 016110.

128 K. Zhao, W. L. Wang, J. Gregoire, M. Pharr, Z. Suo, J. Vlassak and E. Kaxiras, *Nano Lett.*, 2011, **11**, 2962–2967.

129 A. S. Arico, P. Bruce, B. Scrosati, J. M. Tarascon and W. Van Schalkwijk, *Nat. Mater.*, 2005, **4**, 366–377.